Kristín Martha Hákonardóttir
Andrew Hogg, CEGF
Tómas Jóhannesson

A laboratory study of the interaction between supercritical, shallow flows and dams

Abstract

We report on a series of laboratory experiments to study the deflecting and retarding effect of avalanche defence measures. We find that incompressible, shallow-layer shock dynamics can be used to describe the interaction of high Froude number, steady, dense, granular flows with obstacles, such as deflecting and catching dams. Stationary, oblique shocks are formed in the interaction of the flows with deflecting dams, while a travelling bore is formed upstream of a catching dam when none of the flow over-tops the dam. As the height of the dam is lowered compared with the depth of the approaching flow, the bore slows down and finally the flow jumps ballistically over the dam and a shock is not formed upstream of the dam.

Contents

1 Introduction

The traditional design of dams used to deflect or stop dense snow avalanches has been based on simple considerations of the energy of a small part of the flow or the run-up of a point-mass on the upstream facing, sloping side of a deflecting or a catching dam (Irgens *et al.*, 1998). McClung and Mears (1995) consider the run-up onto a catching dam and by accounting for the pressures in the flow, conclude that the point mass theory underestimates the run-up by a factor of two. Both of the approaches, however, may be too idealised. Chu *et al.* (1995) have performed small-scale experiments and tested the theory of McClung and Mears against their observations. Both theories suggest that energy is lost in the impact of the current with the dam and McClung and Mears hypothesise that the flow loses the normal component of its approach velocity in the interaction. A fundamental difficulty with the point-mass view of the impact of an avalanche on a deflecting dam is caused by the finite width of the avalanche, since the lateral interaction of different parts of the avalanche is ignored. The point-mass trajectories corresponding to different lateral parts of the avalanche must intersect as already deflected material on its way down the dam side meets with material heading towards the dam farther down. The effect of this interaction on the run-up cannot be studied easily using a point-mass consideration and a more complete physical description of lateral interaction in the impact process must be developed.

More recent chute experiments and theoretical analysis (Tai *et al.*, 2001, and Gray *et al.*, 2003) suggest a different flow behaviour in the impact of dense supercritical granular flow with obstacles. The experiments indicate that a shock (or a jump) is formed upstream of an obstacle and in the direction normal to the shock, a jump from a supercritical flow state to a subcritical one occurs which may be modelled by 'shallow-water' jump conditions, see for example (Whitham, 1999). Observations of two natural, snow avalanches hitting deflecting dams above the village Flateyri in western Iceland (Jóhannesson, 2001) reveal the same phenomena as these laboratory experiments. The avalanche debris that was left behind showed that the impact had channelised a part of, or the whole of the width of both the avalanches into thicker streams, travelling parallel to the dam and thereby increased the run-out of the avalanches significantly. These observations suggest that a shock was formed near the dams in the interaction.

The fundamental difference between the theoretical approaches described above indicates that further investigations of the behaviour of granular flows interacting with dams are needed. Such studies provide a better understanding of the dynamics of the flows. Small-scale laboratory experiments, larger-scale experiments with snow as well as observations of natural avalanches that hit dams are needed as a part of such investigations.

Three sets of experiments in small-scale laboratory chutes are described in this report. The experiments involve supercritical, dry, dense, granular flows, short and long in duration, on steep slopes and supercritical flow of water on shallow slopes. The experiments were scaled with the internal Froude number of the flows, $\mathrm{Fr} = u/\sqrt{g^\star h}$, where u is the flow speed, $g^\star = g\cos\xi$ is the component of the gravitational acceleration perpendicular to a

slope inclined at an angle ξ to the horizontal and h is the depth of the flow. The Froude numbers of the flows were in range of 5–15. The experiments at the lower Froude numbers are comparable with experimental results of flows interacting with dams reported by Gray *et al.* (2003). Those can then be compared with the higher Froude number flows in order to draw conclusions about the expected flow behaviour in the interaction of the dense core of a natural, dry-snow avalanche with dams.

The dense core of a natural, dry-snow avalanche has a Froude number of the order 10 (Hopfinger, 1983 and Issler, 2003). The compressibility of the dense core, characterised by the Mach number of the flow, Ma, is not well understood (Issler, 2003). The Mach number represents the ratio between the flow speed and the speed of pressure disturbances in the flow (speed of sound in the flow, c), $\mathrm{Ma} = u/c$. In relatively incompressible and shallow free surface flows, pressure disturbances travel as gravity waves on the free surface of the flow with a speed of $\sqrt{gh}$, and the flow is characterised by the Froude number. The shock angle of the avalanche that was partly channelised by the deflecting dam in Flateyri was small and the channelised part of the shock was considerably thicker than the undisturbed part of the flow. The increased flow depth of the shock indicates that the dense core of the avalanche was not highly compressible and the small shock angle is consistent with a high Froude number flow $(\mathrm{Fr}_1 \sim 10)$. We therefore study the behaviour of the dense core by analogy with high Froude number, incompressible flows, though that may not apply to all natural, dry-snow avalanches.

The report starts with a short review and discussion of incompressible, shallow-layer shock dynamics, needed to explain the experimental results (§ 2), followed by a description of the three experimental series. The first series (§ 3) involves an initial set of experiments of granular flows at Froude numbers of the order 10, conducted to identify the flow behaviour in the interaction with a deflecting dam. The avalanches in this series had a short flow duration, that is the length to depth ratio of the currents was approximately 200. The experimental observations gave rise to questions that were addressed in the following two experimental sets where avalanches with a longer flow duration were used (a length to depth ratio of over 10000). Steady water experiments of flows on shallow slopes with Froude numbers close to 5 are described in § 4. They were designed to investigate how well the shallow-water model and the jump conditions agreed with shallow-water experiments. The final set of experiments is described in § 5. The experiments involved steady granular flows at three different Froude numbers; 5, 12 and 14, linking the previous two experimental sets. The three experimental sets are finally compared in § 6 and some general conclusions are drawn from the combined experiments.

8

2   Shock theory

One approach to modelling the interaction of an avalanche with a dam involves viewing the avalanche motion as a stream of supercritical shallow-water that undergoes changes in flow state (hydraulic jump) when interacting with dams. Jumps between flow states have been observed experimentally with dense granular flows down channels (Savage, 1979) and as a result of the interaction with catching and deflecting dams in the laboratory (Gray *et al.*, 2003) and in nature when a snow avalanche of volume 10^5 m^3 hit a deflecting dam in Flateyri, Iceland, in 1999 (Jóhannesson, 2001).

The description of the interaction between granular flow and an obstacle in terms of the dynamics of shallow-water flow involves a dramatic simplification of the physical processes that may not provide an accurate description of flows of natural snow avalanches. The theory is developed below in considerable detail in order to provide a consistent framework for the interpretation of the experiments that have been carried out. Deviations from the predictions of this theory can then provide a starting point for a more realistic theoretical description.

2.1   Classical hydraulic jump
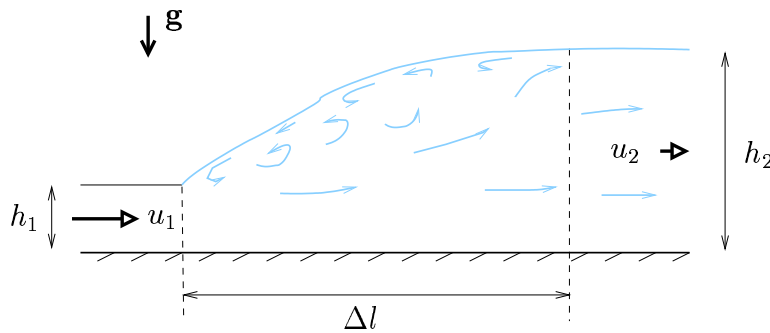
PSfrag replacements

Figure 1: Schematic diagram of a classical hydraulic jump.

Hydraulic jumps are regions where shallow-water flows change from a supercritical to a subcritical state and thereby dissipate mechanical energy. The transition between the two states does not occur abruptly, but rather over a finite length, Δl, illustrated in Figure 1, hereafter referred to as the 'transition zone'.

The characteristics of the hydraulic jump are highly dependent on the Froude number of the approaching flow, Fr_1. Hager (1992) classifies hydraulic jumps according to the magnitude of Fr_1 as follows: The hydraulic jump is termed pre-jump for $1.7 < \mathrm{Fr}_1 < 2.5$. A series of small rollers develop on the surface for $\mathrm{Fr}_1 \sim 1.7$, and are slightly intensified for increasing Froude numbers. The water surface is quite smooth, and the velocity distribution in the tailwater is fairly uniform. Transition jumps correspond to Froude numbers between 2.5 and

4.5. This type of jump has a pulsating action. The entering jet oscillates heavily from the bottom to the surface. Each oscillation produces a large wave of an irregular period. Jumps for $4.5 < \mathrm{Fr}_1 < 9$ are stabilised jumps with the since they have a limited tailwater wave action, a relatively high energy dissipation, and a compact and stable appearance. For extremely high speed flows at Froude numbers above 9, the high velocity jet is no longer able to remain near the underlying boundary. Slugs of water rolling down the front face of the jump intermittently fall into the high-velocity jet and generate additional tailwater waves. The surface of the jump is usually very rough and contains a considerable amount of spray.

According to the classical analysis of two-dimensional hydraulic jumps of a fluid with isotropic, hydrostatic pressure distributions, mass and momentum fluxes are conserved across the jump but mechanical energy is dissipated, see *e.g.* (Whitham, 1999). The analysis describes the conditions on either side of the transition zone but does not resolve the complicated three-dimensional structure of the transition zone. Jump brackets, $[\![\ ]\!]$, are commonly used to indicate differences in flow states upstream and downstream of the jump. The conservation of mass and momentum fluxes across the stationary jump in Figure 1 can be written as

$$
\begin{aligned}
[\![\, u h \rho \,]\!] &= 0, \\
\left[\!\left[h \rho u^2 + \frac{1}{2} g^\star \rho h^2 \right]\!\right] &= 0.
\end{aligned}
\tag{1}
$$

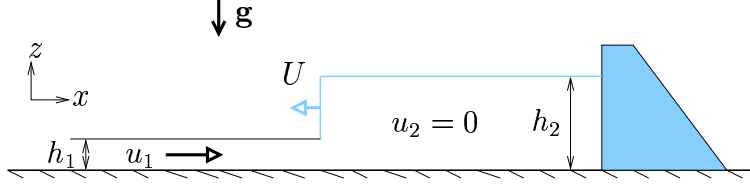PSfrag replacements

2.2 Normal shocks: Catching dams

Figure 2: Schematic diagram of a two-dimensional bore travelling upstream from a catching dam.

When supercrtitical flow passes over an obstacle that is high enough so that the flow state changes to a subcritical state, fluid starts to pile up upstream of the obstacle. The transition between a supercritical flow and a subcritical flow is accomplished in a hydraulic jump, as mentioned above. Figure 2 shows a hydraulic or a granular jump formed when the approaching flow hits a catching dam. A bore travels upstream from the dam and the dam is higher than the depth of the bore. By choosing a reference frame travelling with the bore at speed U to the left, conservation of mass- and momentum fluxes across the jump becomes

$$
\left(u_1 + U \right) h_1 \rho_1 = U h_2 \rho_2,
\tag{2}
$$

$$
h_1 \rho_1 \left(u_1 + U \right)^2 + \frac{1}{2} g^\star \rho_1 h_1^2 = h_2 \rho_2 U^2 + \frac{1}{2} g^\star \rho_2 h_2^2,
\tag{3}
$$

10

where $g^\star = g$ is the acceleration due to gravity and ρ is the density of the flow. For incompressible jumps, such as hydraulic jumps, $\rho_1 = \rho_2$. For granular materials we expect, on the other hand, the stationary material downstream of a jump to be somewhat more closely packed than the dilated flowing material implying $\rho_2 > \rho_1$. An expression, relating the ratio of the shock depth and the depth of the approaching stream to the Froude number of the oncoming flow and the density ratio, ρ_2/ρ_1, is given by

$$\mathrm{Fr}_1 = \frac{h_2}{h_1} \sqrt{\frac{1}{2}\left(\rho_2/\rho_1 - \frac{1}{h_2/h_1} - \left(\frac{1}{h_2/h_1}\right)^2 + \left(\frac{1}{h_2/h_1}\right)^3 \frac{1}{\rho_2/\rho_1}\right)}. \tag{4}$$

The ratio, h_2/h_1, is plotted in Figure 3 (a) as a function of Fr_1 for different density ratios. Increased density difference lowers the height of the bore. The Froude number of the incoming flow can, furthermore, be obtained as a function of the ratio of the bore speed and the speed of the approaching flow and the density ratio

$$\mathrm{Fr}_1 = \frac{1}{U/u_1} \sqrt{\frac{1 + 2U/u_1 - (\rho_2/\rho_1 - 1)(U/u_1)^2}{2\rho_2/\rho_1(1 + U/u_1)}}. \tag{5}$$

The function is plotted in Figure 3 (b) for different density ratios. We note that at high upstream Froude numbers, the bore speed is slow compared with the speed of the incoming flow and the increased density difference slows the bore down.

The same set of equations with $g^\star = g\cos\xi$ (the component of gravity normal to a slope inclined at an angle ξ to the horizontal) may be used to describe flow down an inclined plane,
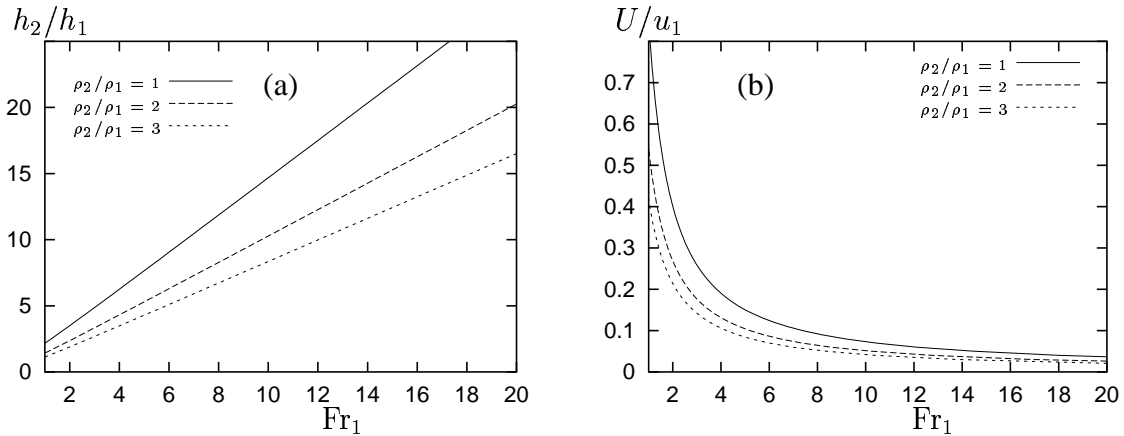

Figure 3: The ratio between the bore speed and the speed of the incoming flow as a function of the Froude number. The density ratios between 1 and 3 are chosen to correspond to possible density ratios in snow avalanches. Issler (2003) suggests that the dense core of a flowing dry-snow avalanche has a density in the range $\rho_1 = 250$–$500\,\mathrm{kg\,m}^3$ while the density of avalanche debris hardly exceeds $\rho_2 = 500$–$600\,\mathrm{kg\,m}^3$.
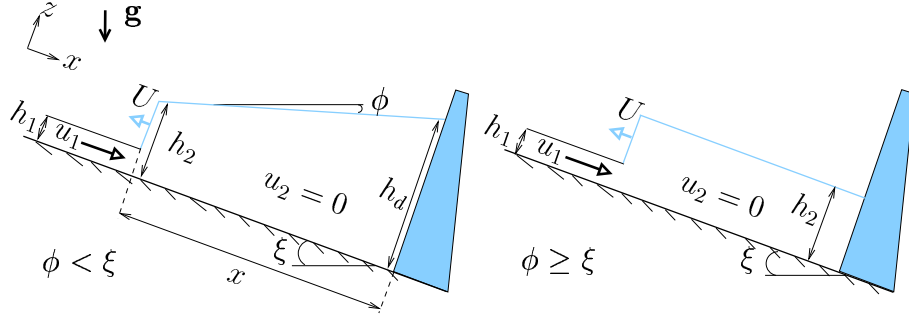
11

Figure 4: Schematic diagram of a bore travelling up an inclined plane, away from a catching dam, for material with different internal friction angles ϕ.

interacting with a dam, when the internal friction angle of the stationary material is larger than or equal to the slope angle, $\phi \geq \xi$. This will be the case if the transition zone is thin enough so that the component of gravity along the slope (the additional accelerative term, $g \sin \xi$) will not affect the conservation of momentum flux over the bore, see Figure 4. The free surface of a stationary pile of material is stable at angles up to the internal friction angle of the stationary pile, this angle is also termed the angle of repose of the material, ϕ. The free surface of the stationary material downstream of the shock is therefore stable at the slope angle ξ if $\phi \geq \xi$ and arrests on the slope downstream of the bore with the surface inclined at ξ. That implies that the depth of the stationary material in front of the dam is h_2 everywhere. In the case of material with $\phi < \xi$ ($\phi = 0$ for fluids), the stationary material (fluid) arrests on the slope downstream of the bore with the free surface inclined at the angle of repose and the depth of the stationary material just in front of the dam, h_d, increases the further upstream the bore travels. The mass flux, previously described by equation (2), needs to be adjusted in order to account for the the redistribution of the mass that is stopped in front of the dam

$$
\begin{aligned}
u_1 h_1 \rho_1 + \frac{\partial}{\partial t}\left(\rho_1 h_1 x\right) &= \frac{\partial}{\partial t}\left(\left[h_2 + \frac{h_d - h_2}{2}\right]\rho_2 x\right), \\
\left(u_1 + U\right) h_1 \rho_1 &= U \rho_2 \left(h_2 + x \tan\left(\xi - \phi\right)\right),
\end{aligned}
\tag{6}
$$

where x is the position of the front of the bore, $h_d = h_2 + x \tan\left(\xi - \phi\right)$ and $\partial x / \partial t = U$.

As the height of the catching dam decreases relative to the depth of the approaching stream, some flow will escape over the dam and reach a critical state at the top of the dam, see *e.g.* (Gerhart *et al.*, 1993), while a hydraulic/granular jump is still present upstream of the dam, see Figure 5 (a). More of the flow escapes over the dam if the height of the dam is decreased further and finally a bore can no longer be maintained upstream of the dam and the flow jumps supercritically over the dam, as shown in Figure 5 (b).

The hydraulic/granular jump upstream of a dam with overflow, positioned on a slope inclined at an angle ξ with $\phi \geq \xi$ can be calculated by considering the conservation of mass and
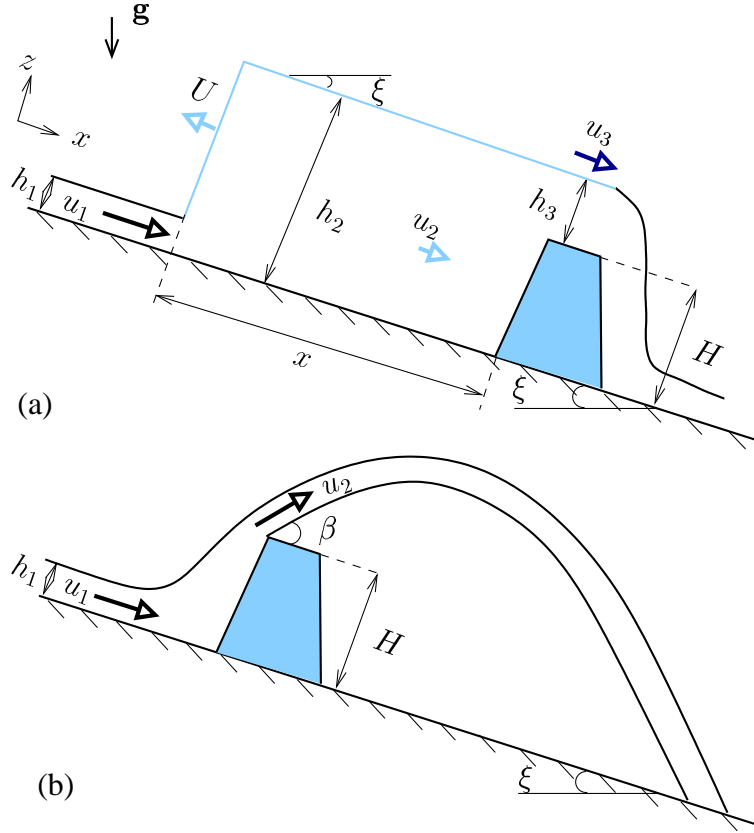
12

(a)

(a)

(b)

Figure 5: The top figure (a) is a schematic diagram of a granular jump formed upstream of a dam, when supercritical flow interacts with the dam, some of the flow escapes over the dam. The flow over the dam is critical, $\mathrm{Fr}_3 = 1$, $U > 0$, $\phi \geq \xi$. The bottom figure (b) shows supercritical flow jumping over a dam, $U < 0$.

momentum fluxes across the bore in a reference frame travelling with the bore

$$(u_1 + U) h_1 = (u_2 + U) h_2, \tag{7}$$

$$\frac{1}{2} g^\star h_1^2 + (u_1 + U)^2 h_1 = \frac{1}{2} g^\star h_2^2 + (u_2 + U)^2 h_2. \tag{8}$$

We have assumed that $\rho_1 = \rho_2 = \rho_3$ for simplicity, since the flow does not stop completely in front of the dam and will therefore not be as closely packed as in the case of no over-topping. Conservation of mass flux over the dam in a stationary frame of reference becomes

$$h_2 u_2 = h_3 u_3 \qquad \text{where} \qquad h_3 = h_2 - H, \tag{9}$$

by, for simplicity, assuming that the flow is in a constant, uniform state downstream of the jump, *i.e.* the downslope component of gravity is balanced by friction. The flow goes through

13

another transition of state as it passes over the dam. It is subcritical upstream of the dam and supercritical downstream of the dam. We therefore find that the flow over the dam is critical, leading to a final constraint on the flow:

$$\text{Fr}_3 = 1, \qquad \text{which implies that} \qquad u_3 = \sqrt{g^\star h_3}. \tag{10}$$

In the case of material with $\phi < \xi$, the free surface of the granular material is stable at the angle of repose if u_2 is sufficiently small and equation (9) becomes

$$(h_2 + x \tan(\xi - \phi)) u_2 = h_3 u_3 \qquad \text{where} \qquad h_3 = h_2 + x \tan(\xi - \phi) - H, \tag{11}$$

PSfrag replacements
and x is the distance from the front of the bore to the catching dam, see Figures 4 and 5 (a).

A hydraulic/granular jump can no longer be maintained upstream of the dam when the computed speed of the bore becomes negative and the flow jumps over the dam in a supercritical flow state. The jet takes a ballistic trajectory over the dam as described by Hákonardóttir *et al.* (2003a and 2003b) for flows with braking mounds and catching dams in which the obstacles have a height comparable to the depth of the approaching flow.

2.3   Oblique shocks: Deflecting dams

$$\mathbf{u_1} = (u_1, 0)$$
$$\mathbf{u_2} = (u_2 \cos\gamma, u_2 \sin\gamma)$$
$$\hat{\mathbf{n}} = (-\sin\beta, \cos\beta)$$
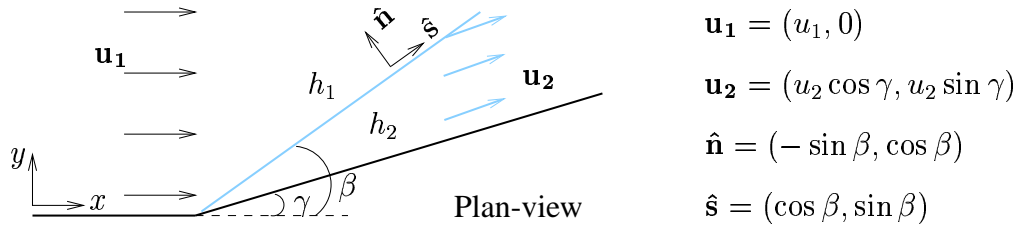$$\hat{\mathbf{s}} = (\cos\beta, \sin\beta)$$

Figure 6: Uniform fluid flow hits a deflecting dam at an angle γ and a stationary, oblique shock is formed at an angle β to the incoming flow. Unit vectors normal and tangential to the shock are denoted by $\hat{\mathbf{n}}$ and $\hat{\mathbf{s}}$. The flow downstream of the shock is parallel to the dam.

Shock conditions can be formulated for fluid flow hitting a deflecting dam and forming an oblique, stationary shock that is flowing with a constant speed in a direction parallel to the dam. These conditions can be obtained in most text books on gas dynamics, *e.g.* (Whitham, 1999), and adapted to shallow-water flow. We assume that $\rho_1 = \rho_2$ in the granular flow, since the flow on both sides of the shock is in a dilated flowing state. The conservation of mass flux across the jump takes the form

$$[\![\, h\mathbf{u} \cdot \hat{\mathbf{n}} \,]\!] = 0,$$

which leads to

$$h_2 u_2 \sin(\beta - \gamma) = h_1 u_1 \sin\beta. \tag{12}$$

14

Conservation of momentum flux across the jump can be written as

$$\left[\!\left[h\mathbf{u}\left(\mathbf{u}\cdot\hat{\mathbf{n}}\right) + \frac{1}{2}g^{\star}h^{2}\hat{\mathbf{n}} \right]\!\right] = 0,$$

which in the directions normal and tangential to the shock becomes

$$\frac{1}{2}g^{\star}h_{2}^{2} + h_{2}u_{2}^{2}\sin^{2}\left(\beta-\gamma\right) = \frac{1}{2}g^{\star}h_{1}^{2} + h_{1}u_{1}^{2}\sin^{2}\beta, \tag{13}$$

$$h_{2}u_{2}^{2}\sin\left(\beta-\gamma\right)\cos\left(\beta-\gamma\right) = h_{1}u_{1}^{2}\sin\beta\cos\beta. \tag{14}$$

Equation (14) together with (12) implies that the speed along the shock must be continuous

$$u_{2}\cos\left(\beta-\gamma\right) = u_{1}\cos\beta.$$

By solving (12), (13) and (14) for a given incoming speed and flow depth, the outgoing flow speed and depth can be calculated along with the oblique shock angle, β. An expression, relating the shock angle to the known flow parameters (the Froude number of the flow and the deflecting angle of the dam) is given by

$$\mathrm{Fr}_{1} = \frac{1}{\sin\beta}\sqrt{\frac{\tan\beta}{2\tan\left(\beta-\gamma\right)}\left(\frac{\tan\beta}{\tan\left(\beta-\gamma\right)}+1\right)}. \tag{15}$$

For a given Froude number and a given deflecting angle, there are two possible shock angles. The smaller angle corresponds to a weak shock and the larger one to a strong shock. As $\gamma \to 0$ the weak shock tends to $\beta = \sin^{-1}\left(1/\mathrm{Fr}_{1}\right)$ and the strong shock tends to a normal shock, for which $\beta = 90°$. The flow speed downstream of a weak shock is nearly always supersonic, while the speed becomes subsonic through a strong shock. We restrict our discussion to weak shocks since those are the ones that usually occur in practice. Using equation (15), we plot the behaviour of the shock angle relative to the dam as a function of the Froude number for constant deflecting angles in Figure 7 (a) and as a function of the deflecting angle for constant Froude numbers in Figure 7 (b). The plots indicate that the shock angle is highly dependent upon the Froude number of the flow and becomes smaller with increasing Froude number. We furthermore note that for high Froude numbers, the shock angle is relatively independent of the deflecting angle of the dams. The ratio between the shock height and the depth of the approaching stream is plotted as a function of the Froude number for constant deflecting angles in Figure 7 (c) and as a function of the deflecting angle for constant Froude numbers in Figure 7 (d). The plots show that the shock depth increases with increasing deflecting angles and Froude numbers.

In this analysis, the pressure in the granular material has been assumed to be hydrostatic and isotropic. There is a debate in the granular flow literature about whether the assumption of an isotropic pressure field is appropriate for granular flows such as snow avalanches. For
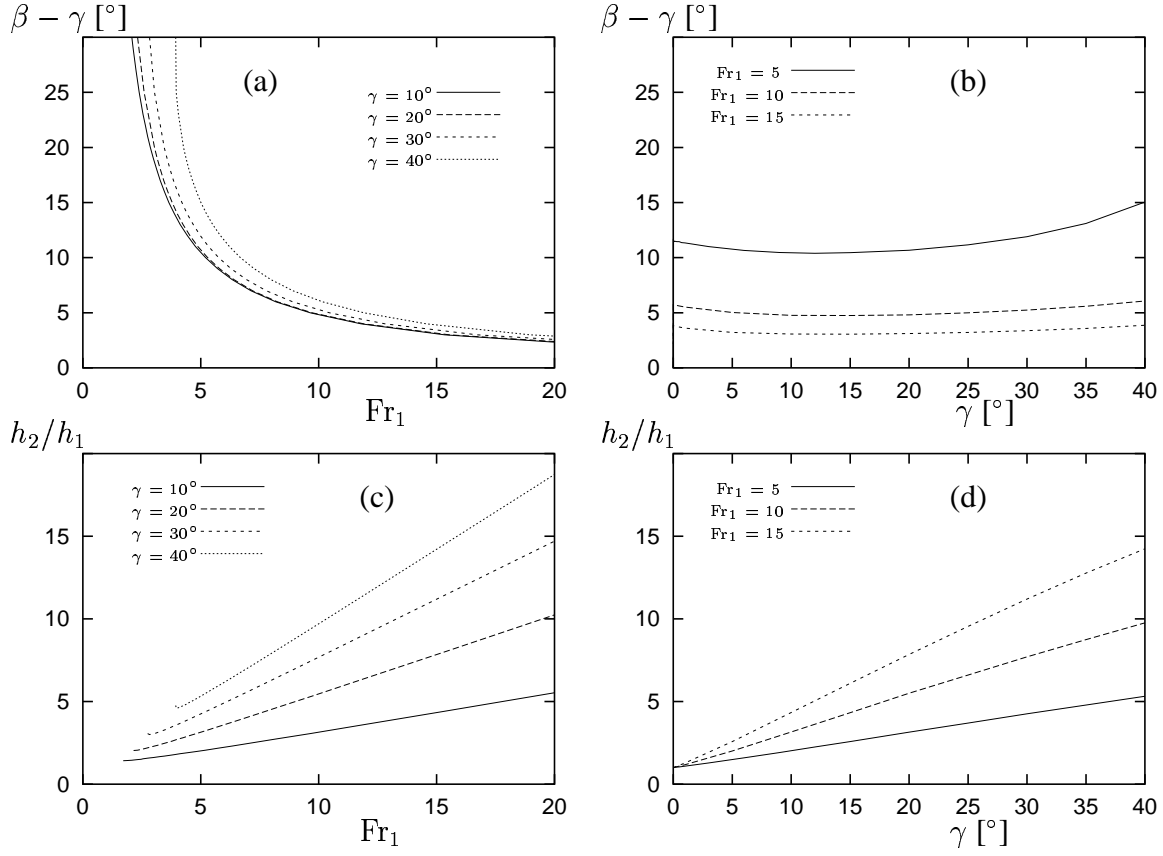
15

$\beta - \gamma$ [°]

(a)

$\gamma = 10°$ ———
$\gamma = 20°$ ------
$\gamma = 30°$ ········
$\gamma = 40°$ ··········

$\beta - \gamma$ [°]

$\mathrm{Fr}_1 = 5$ ———
$\mathrm{Fr}_1 = 10$ ------
$\mathrm{Fr}_1 = 15$ ········

(b)

PSfrag replacements

PSfrag replacements

PSfrag replacements

PSfrag replacements
Fr_1

γ [°]

h_2/h_1

$\gamma = 10°$ ———
$\gamma = 20°$ ------
$\gamma = 30°$ ········
$\gamma = 40°$ ··········

(c)

h_2/h_1

$\mathrm{Fr}_1 = 5$ ———
$\mathrm{Fr}_1 = 10$ ------
$\mathrm{Fr}_1 = 15$ ········

(d)

Fr_1

γ [°]

Figure 7: The shock angle relative to the deflecting dam plotted: (a) as a function of the Froude number for constant deflecting angles and (b) as a function of the deflecting angle for constant Froude numbers. The shock height non-dimensionalised by the depth of the approaching flow plotted: (c) as a function of the Froude number for constant deflecting angles and (d) as a function of the deflecting angle for constant Froude numbers.

example, Savage and Hutter (1989) link the components of the pressure field parallel with and normal to the slope, p_{xx} and p_{zz}, through an earth pressure coefficient, defined by

$$K = \frac{p_{xx}}{p_{zz}}.$$

Values of the earth pressure coefficient may be derived assuming a Mohr-Coulomb plastic behaviour for the cohesionless yield on the basal sliding surface,

$$K = \begin{cases} K_{\mathrm{act}} & \text{for} \quad \partial u/\partial x > 0, \\ K_{\mathrm{pass}} & \text{for} \quad \partial u/\partial x < 0, \end{cases}$$

with

$$K_{\mathrm{act/pass}} = 2\left(1 \mp \sqrt{1 - \cos^2\phi/\cos^2\delta}\right)\sec^2\phi - 1,$$

16

where ϕ is the internal friction angle of the granular material and $\mu = \tan\delta$ is the dynamic friction coefficient at the bed. If the jump conditions (1) are implemented with anisotropic pressure, then the conservation of momentum flux across the bore becomes

$$\left[\!\!\left[h\rho u^2 + \frac{1}{2}K_{\text{pass}}g^\star\rho h^2 \right]\!\!\right] = 0. \tag{16}$$

Gray *et al.* (2003) and Pouliquen and Forterre (2002) treat the pressure in granular flows as isotropic and hydrostatic and obtain better agreement with the experimental results than when using an earth pressure coefficient. Gray *et al.* also argue that the discontinuity in the pressure, introduced through the earth pressure coefficient, is unphysical and should lead to a discontinuity in the flow depth. They base their theoretical model on older models of avalanches, developed by Russian scientists, see *e.g.* (Eglit, 1983), where direct analogy is made between granular avalanches and shallow-water flows.

3 Laboratory experiments of short duration, steady granular flows interacting with deflecting dams

The experiments were designed to study the deflection of high Froude number granular flow by a dam and to compare the flow behaviour in the interaction with the dam with the point mass theory and the shallow-water theory, described in § 2. The necessary height of a deflecting dam at a constant deflecting angle, needed to fully deflect the oncoming flow, was quantified and the flow behaviour if some of the flow escaped over the dam was studied.

3.1 Experimental setup and design

The experiments were performed on a 6 m long wooden chute consisting of two straight sections, one inclined at $38°$ to the horizontal and the other one horizontal, see Figure 3.1. The sections were connected by a thin plywood sheet, positioned 2.32 m downslope from the gate, to obtain a smooth transition between the sections. The chute had 0.20 m high side walls made of perspex to allow for recording from the sides.

The deflecting dams were constructed of plywood and positioned at the upper section of the chute, 1.69 m downslope from the gate perpendicular to the base of the chute, at five different deflecting angles to the flow; $\gamma = 8$ °, $15°$, $24°$, $32°$ and $44°$, see Figure 8. The dams had a flow depth to dam height ratio from 1 to 20, or up to the dam height needed to fully deflect the flow for each deflecting angle.

The experiments were designed so that the granular current had an internal Froude number of the order 10. Glass beads (ballotini) of mean size $90\,\mu$m, density $2500\,\mathrm{kg\,m^{-3}}$ (bulk density of $1600\,\mathrm{kg\,m^{-3}}$) and an approximately spherical shape were used. In each experiment, 6 kg of particles were released from the top of the chute by the rapid opening of a lock gate. The interaction between the flow and the deflecting dams was recorded from above and from the side with two video cameras. The evolution of the depth profile on the deflecting dams was measured by analysing the side-view video footage of the experiments. The angles of the deflected and the overflowing parts of the stream to the deflecting dam were analysed from the video footage provided by the camera that was positioned above the dams. The run-out length and distribution of the deposited particles were also measured.

The speed of the flow in front of the dams was measured over a length of 0.40 m by tracking the first front of the flow and tracer particles for interior speeds. The maximum flow depth was measured by fixing a gate in the flow path at a known distance from the base of the chute. The distance of the gate from the chute was then increased systematically until all of the current flowed under the gate without touching it.
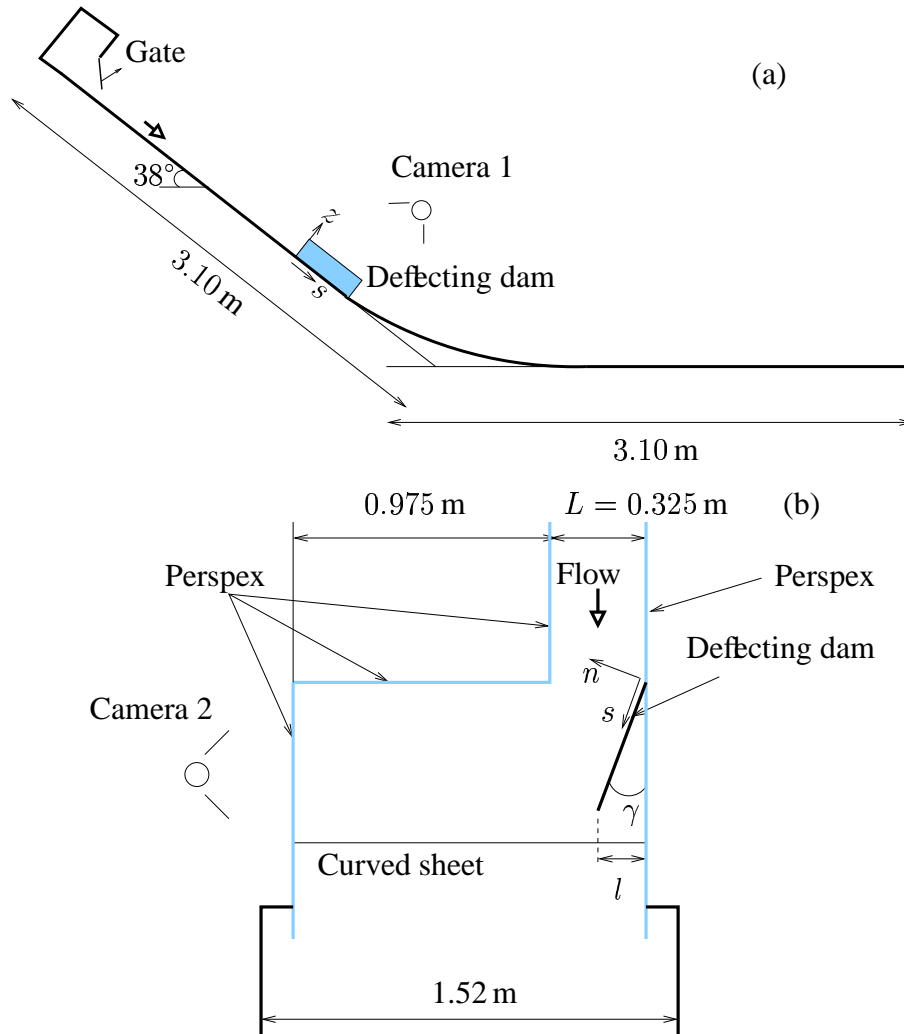
Figure 8: Schematic diagrams of the experimental chute, (a) shows a side-view of the chute and (b) a plan-view of the chute section next to the deflecting dam. The run-out zone starts were the slope angle changes, at the curved sheet. The channelled section of the chute is approximately 1.70 m long, measured from the lock gate.

3.2   Flow description

The flow quickly reached a terminal velocity on the upper section of the chute and flowed down the chute with a constant speed and a constant depth. The head of the flow was about 0.50 m long, 0.04 m thick and had a speed of $(3.7 \pm 0.8)\,\mathrm{m\,s^{-1}}$. It was very dilute (it could be seen through when looked at from above) and turbulent, with eddies suspending the glass beads. The flow immediately following was much denser with a constant depth of

19
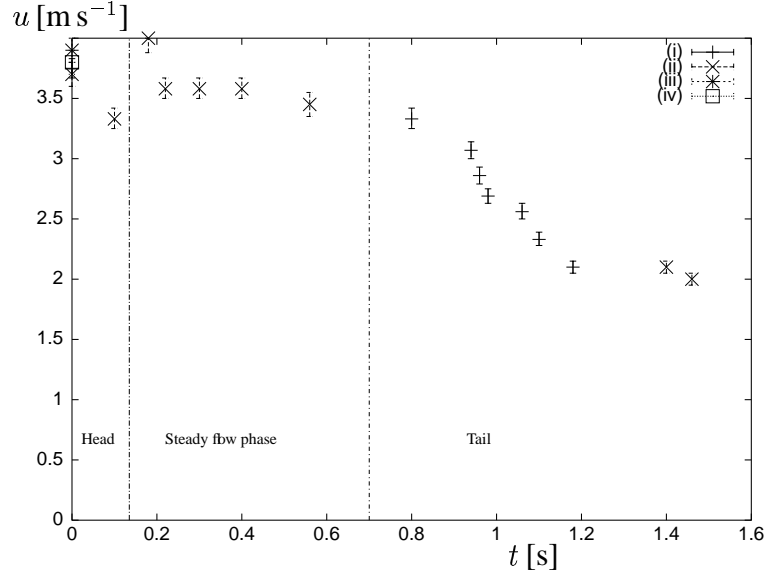
Figure 9: Flow speeds plotted as a function of time for experiments number (i) 83 to (iv) 86. The speed was measured at a fixed position, in front of the deflecting dams.

(0.009 ± 0.001) m and speed of (3.5 ± 0.1) m s^{-1}, resulting in a Froude number of 13. The dense flow phase was maintained for 0.6 s, so the flow was roughly 2.1 m long. This flow phase will be referred to as the steady flow phase. The flow rapidly thinned and slowed down after that, see Figure 9.

During the experimental period the particles changed slightly in character, leading to increased mobility of the flow. The run-out lengthened linearly by approximately 5% during the period, measured from the start of the run-out zone. The front speed of the flow was also found to increase linearly through the experimental period, see Figure 10. The interior speeds (the speed of the steady flow phase) were only measured at the end of the experimental period. It was thus assumed that the steady interior speed increased throughout the experimental period in the same fashion as the front speed, but with a 0.2 m s^{-1} lower speed as Figure 9 suggests. A summary with the exact values of the interior speeds that were used for the different deflecting angles is given in Table 1.

3.3   Results: Flow completely deflected by the dams

The dilute first front splashed onto the deflecting dam up to a similar height as the denser part immediately following and forming a semi-steady profile on the dam. The width of the stream flowing along the dam increased downstream and finally formed a jet at the end of the dam in a direction parallel with the dam. Figure 11 shows that the maximum run-up of the granular avalanches on the dams grew with increasing deflecting angles.

The effect of subjecting larger and smaller proportions of the avalanches to the deflect-
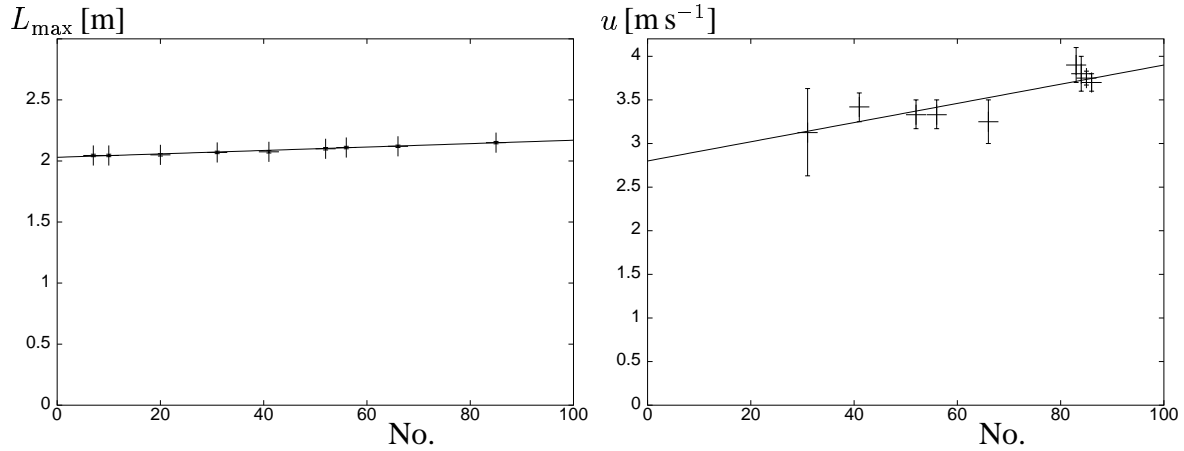
20

Figure 10: The maximum run-out and the front speed plotted as a function of the sequential number of the experiment performed (+) with a linear fit through the observations. The maximum run-out was measured from the start of the run-out zone (the curved sheet).

$\gamma[°]$	No.	$u\,[\mathrm{m\,s^{-1}}]$
8.0 ± 0.5	65	3.3
15.0 ± 0.5	60	3.3
24.0 ± 0.5	47	3.1
32.0 ± 0.5	39	3.0
44.0 ± 0.5	55	3.2
90.0 ± 0.1	11	2.7

Table 1: The estimated interior speed of the flow, u, during the steady flow phase for the different deflecting angles, γ. The number of each experiment is denoted by No.

ing dams on the run-up on the dams (long and short dams) was examined for three different deflecting angles. Figure 12 shows a plot of the locus of the maximum run-up onto the deflecting dams for deflecting dams covering different proportions of the width of the avalanche, $0.2 \leq l/L \leq 1.1$, where L is the width of the avalanche and l is the deflected width defined in Figure 8. The maximum flow depth along the dams was always reached after a distance that was shorter than the length of the dams. Changing the length of the dams did therefore not alter the maximum flow depth in front of the dams. It was furthermore concluded that the end of the dams, where the pressure suddenly drops, did not affect the run-up profiles on the dams significantly, which is consistent with the flow being in a supercritical flow state along the dams.
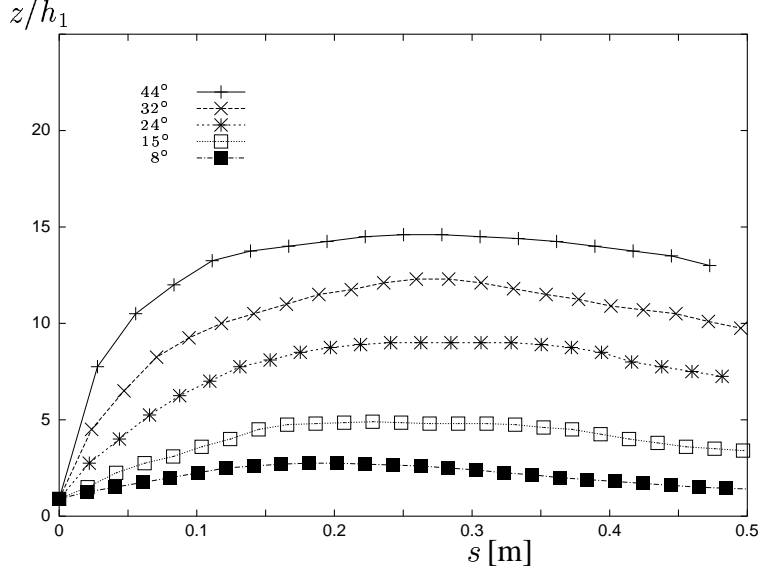
Figure 11: The locus of the maximum run-up on the deflecting dams non-dimensionalised with the thickness of the incoming stream plotted as a function of the length along the dams for the different deflecting angles. The uncertainty in the non-dimensional run-up is estimated ± 1 due to the short duration of the steady flow phase and an inaccuracy in drawing/visualising the curves from the video recordings.

3.3.1 Comparison with existing theories

The point mass model (PM), developed by Irgens *et al.* (1998), was used to calculate the path of a point-mass along a deflecting dam, assuming no loss of energy in the impact with the dam. The Coulomb friction parameter in the model, μ, was taken to be $\mu = \tan \delta$, where δ is the dynamic friction angle between the flow and the base of the experimental chute which was measured to be about $20°$, implying $\mu \approx 0.4$. The dimensional coefficient representing turbulent dissipation, M/D, can be determined from the steady state of the momentum equation, see Irgens *et al.* (1998)

$$u^2 = (M/D)g(\sin \xi - \mu \cos \xi). \tag{17}$$

By substituting the measured, steady flow speed and depth on the chute into equation (17) we obtain $M/D \approx 4\,\mathrm{m}$. The physical range of these parameters for snow is discussed by Perla (1980).

Figure 13 shows that for small deflecting angles, the point mass model predicts the run-up on the deflecting dams well, but overshoots when the deflecting angle increases. No parameter values, within a reasonable physical limit of the two parameters, μ and M/D, could reproduce all the observed curves at once. The reason might be that dissipation of the mechanical energy of the flow takes place when the current impacts the dams. The dissipation can be assumed to increase with larger deflecting angles as the velocity component normal to the dams increases.
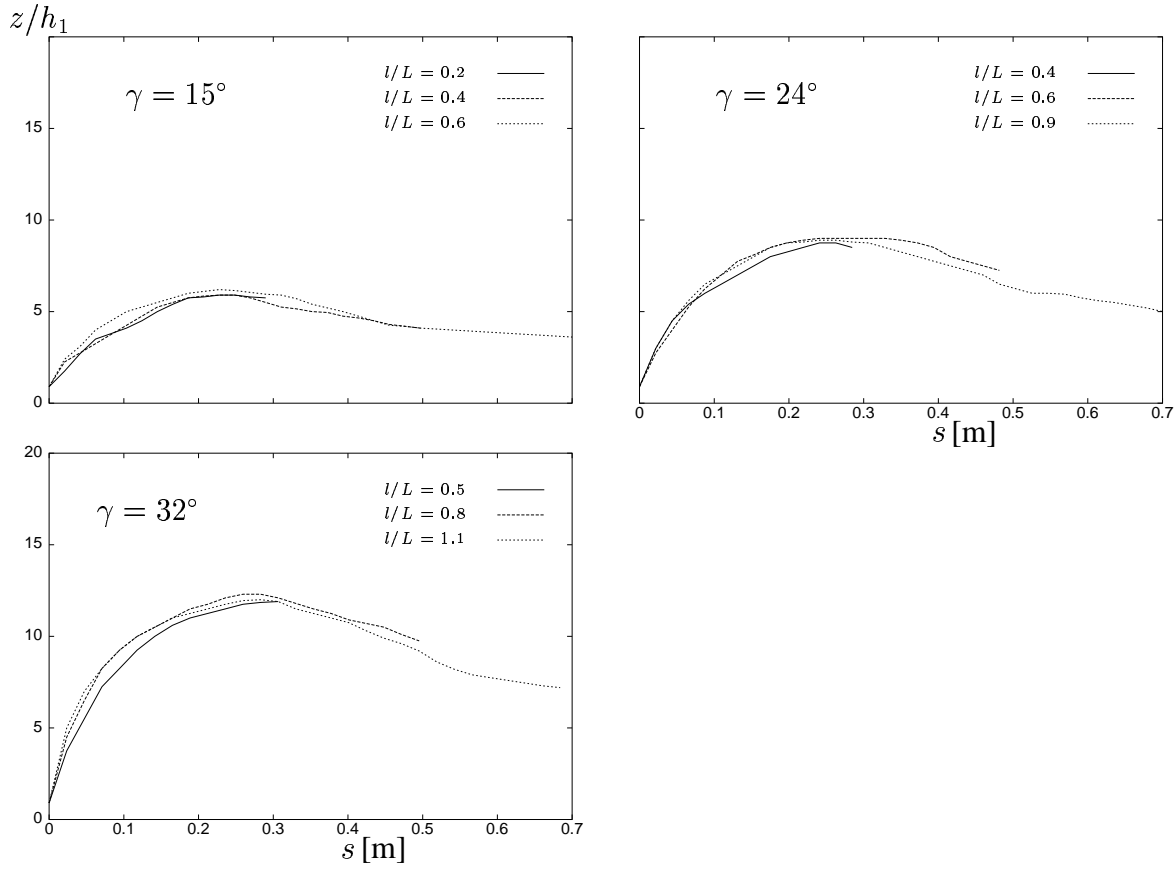
22

Figure 12: The non-dimensional run-up profiles of the avalanches on the deflecting dams plotted as a function of the length along the dams. The deflecting dams covered different proportions of the width of the avalanches, l/L (see Figure 8 for definition), between 0.2 and 1.1. The maximum run-up was reached during the steady flow phase.

If that is the case, tilting of the dams should affect the dissipation and the run-up on the dams. McClung and Mears (1995) account for internal pressure in the flow, which is neglected in the point-mass theory. They find that the run-up onto catching dams becomes twice as high as the point-mass theory predicts. The experiments reported here show the opposite, at least when no additional dissipation is incorporated. McClung and Mears, furthermore, suggest that the flow should lose its velocity component normal to the dam in the impact. That implies that there should not be run-up onto dams that have an upstream face normal to the slope on which they are positioned and is therefore not in agreement with our experimental results. The point mass theory developed by Irgens *et al.* and the more advanced theory by McClung and Mears do not seem to capture the physics of the interaction correctly.
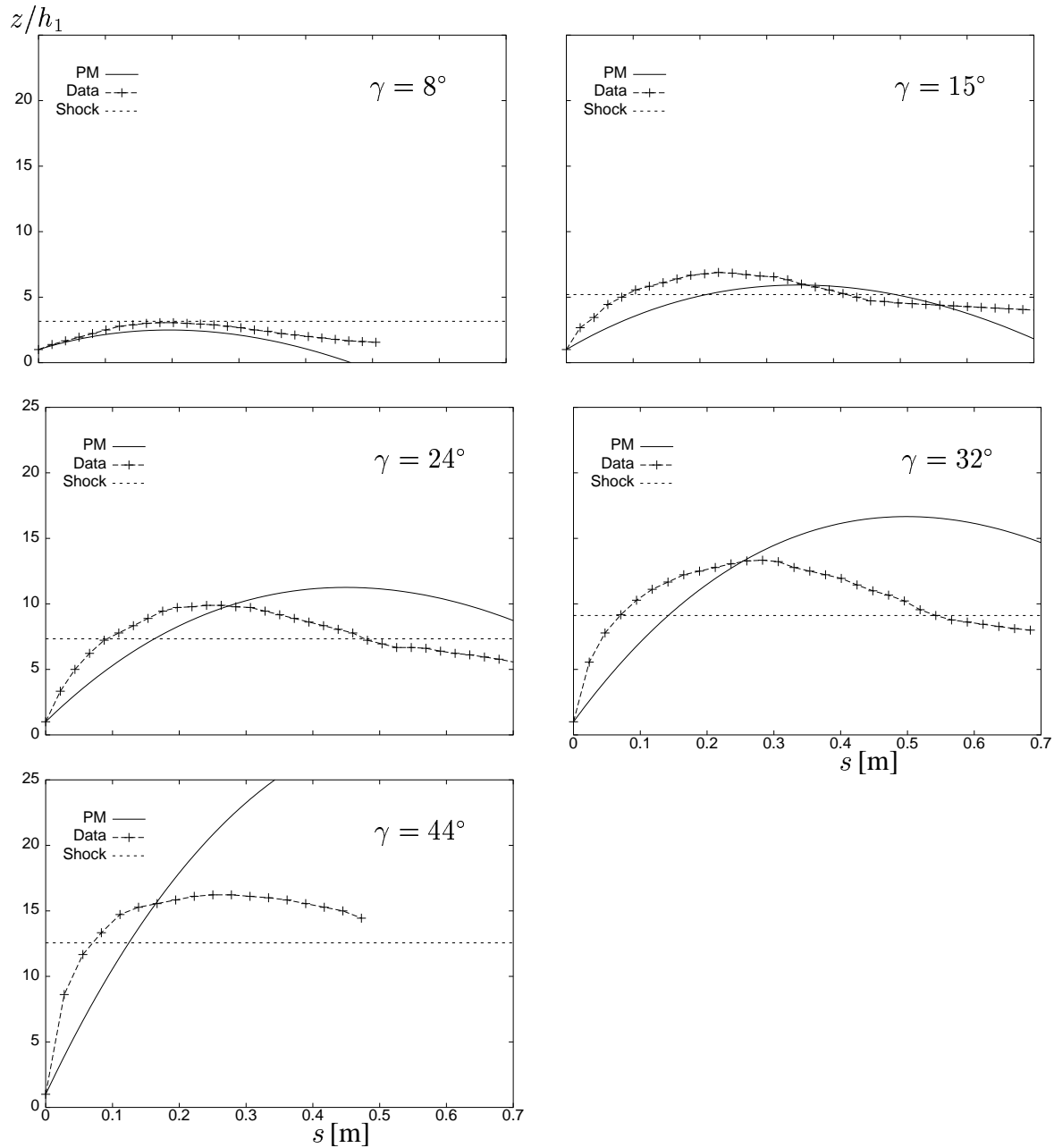
Figure 13: Non-dimensional run-up profiles for granular flows at $\mathrm{Fr}_1 = 13$. Each graph shows the observed depth profile along the deflecting dams, non-dimensionalised with the depth of the approaching stream, for a fixed deflecting angle, γ $(+)$. The theoretical non-dimensional run-up of a point mass is shown with a solid curve and the theoretical non-dimensional shock height with a dashed line.

The granular flow consists of a thin, dense layer of numerous interacting point masses and can therefore be viewed to some approximation as a fluid or gas-like current. The flows are shallow, supercritical and not highly compressible, which gives rise to the possibility of shocks in the flow depth forming upstream of the dams (granular jumps) see the theoretical overview in § 2. The shock height, h_2, was calculated from the shallow-water jump conditions, equations (12), (13), and (14), and is plotted in Figure 13 as a straight line. We see that the observed run-up (+) is initially higher than the predicted shock height. The run-up then decreases along the dams and the theoretically derived shock height predicts the run-up close to the end of the deflecting dams. By introducing an earth pressure coefficient, K, into the jump conditions (equation (16)) the theoretical shock height is lowered, since $K_{\mathrm{act/pass}} > 1$, and worse agreement with the experimental observations is obtained. The theoretical shock angle is plotted in Figure 14 along with the observed widening of the stream along the deflecting dams for the different deflecting angles.

The agreement of the shock theory with the experimental observations indicates that a shock forms upstream of the deflecting dams as is expected for supercritical flow of incompressible fluids interacting with deflectors. What still remains unclear from these experiments is why the flow ran higher up on the dams than the jump conditions predicted and had a tendency to turn over in a backwards rotating motion along the first 0.4–0.5 m of the dams. It is also unclear whether gravity disturbs the shock formation or influences the shock height along the dams, since the experiments were conducted with steady flows on a sloping surface, whereas the theory was derived for fluid flow on a horizontal plane where the flow states on
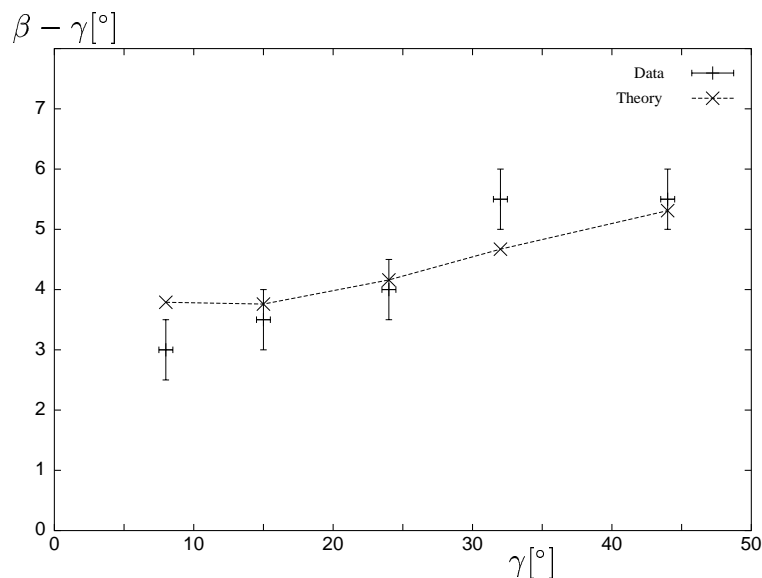

Figure 14: The shock angle relative to the dam, $\beta - \gamma$, plotted as a function of the deflecting angle, γ, for the theory (dashed line) and the experimental observations (+).

25

both sides of the shock are constant. There is furthermore a possibility that friction at the side of the dam affects the relatively narrow shock. The steady state flow phase was also quite short ($\sim 0.6\,\mathrm{s}$) and one wondered whether the run-up onto the dams would develop further for a longer steady flow phase.
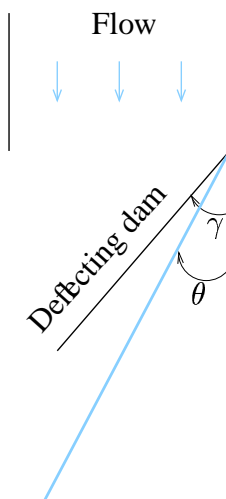
3.4 Results: Flow over-topping the dams

Figure 15: Plan-view of the experimental chute defining the overflow angle, θ.

The over-topping of flow interacting with deflecting dams was investigated by measuring the overflow angle, θ, defined in Figure 15, during the steady flow phase for dams of different heights, H, and at different deflecting angles, γ. When the deflecting dams were not high enough to fully deflect the flow, a part of the flow over-topped the dams. The experiments showed that for very low dams the current shot over the dams in a direction close to that of the approaching stream, $\theta \approx 0$. The jets were then turned more in the direction of the deflecting dams as the dams became higher and the overflow angle of the jets approached the deflecting angles of the dams as the height of the dams approached the height needed to fully deflect the current, *i.e.* $\theta \to \gamma$ for $H \to h_2$, if a shock is formed upstream of the dams. This effect is illustrated in Figure 16 where θ/γ is plotted as a function of H/h_2 for the five deflecting angles.
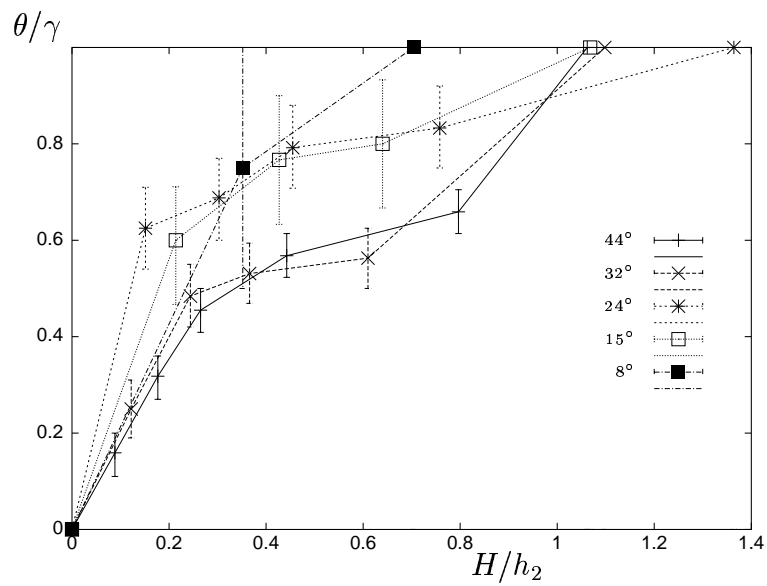
Figure 16: The overflow angle, θ, non-dimensionalised with the deflecting angle, γ, plotted as a function of the ratio between the dam height, H, and the calculated shock height, h_2.

4 Laboratory experiments of steady water flows interacting with deflecting dams

Two series of water experiments were conducted to study how well shallow water shock theory agreed with observations of rapid, shallow water flow.
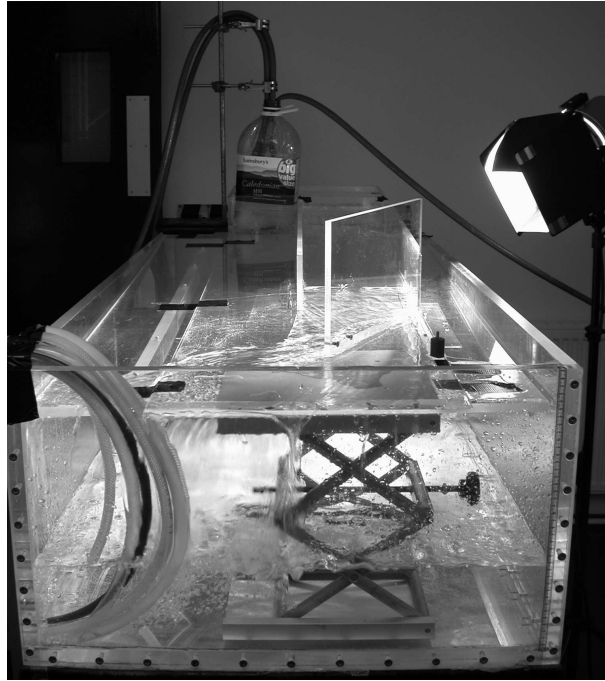
4.1 Experimental setup and design

Figure 17: A photograph of the experimental setup for rapid flows of water. A steady stream of water was supplied through 3 hoses and stored in a reservoir. The water flowed over a weir and under a gate to minimise turbulence and wave action, and continued down a 0.2 m wide perspex channel before finally hitting a deflecting dam, also made of perspex. The deflecting dams were 0.3 m long and did never completely cover the width of the channel.

The experiments involved a steady stream of supercritical water flow down a 0.2 m wide channel at a speed u_1 and a depth h_1. This stream hit a deflecting dam and formed a steady hydraulic jump of height h_2 with speed along the dam, u_2, see Figure 17. The flow ended up in a large tank that gradually filled during the experiments, since the draining system did not fully cope with the flux of water into the tank. It was therefore necessary to split the experiments into two series: one to measure the height of the hydraulic jump and another to

28

measure the deflecting angle. The depth profiles on the dams and the deflecting angles were photographed with a digital camera, through the side of the dams and from above (Figure 18). The depth profiles and shock angles were measured for water flow on three different slopes, inclined at $3°$, $6°$ and $9°$ to the horizontal. The flow speed, u_1, and depth, h_1, upstream of the dams were different for the different channel slopes, and consequently the oncoming flow had different Froude numbers in each of the three different experimental setups.
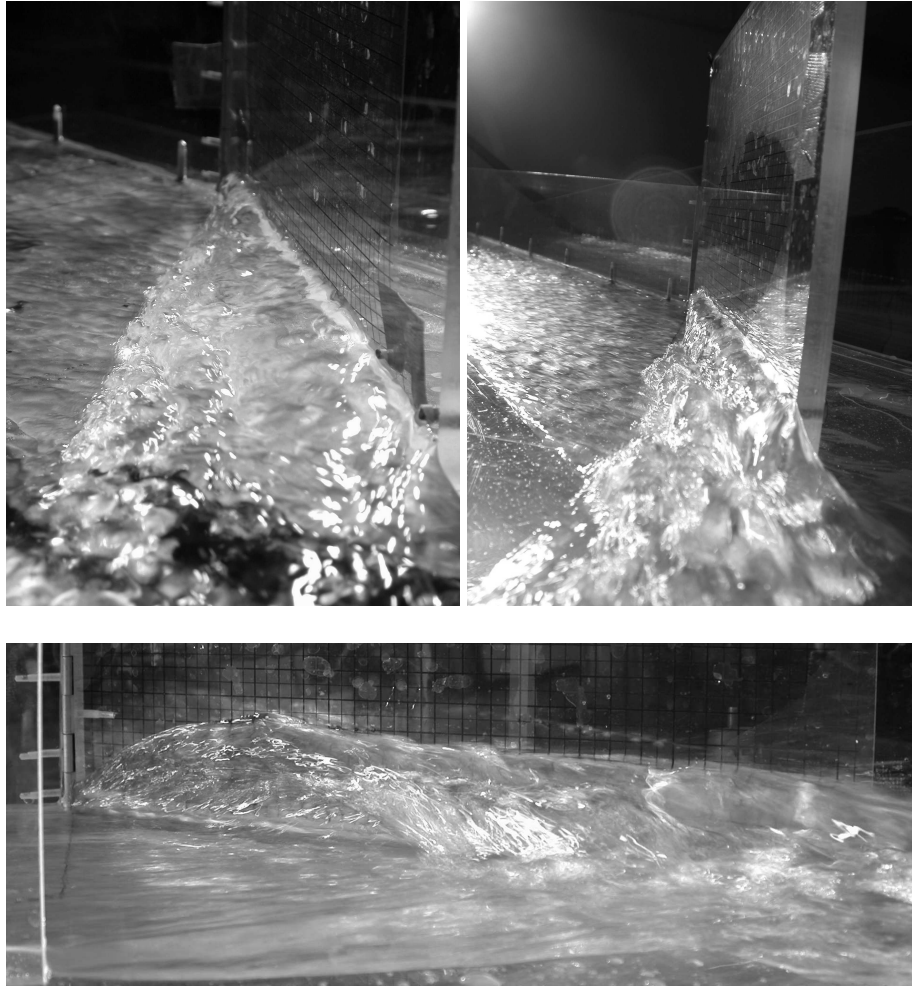

Figure 18: Photographs of stationary, oblique shocks of supercritical shallow water at $\mathrm{Fr}_1 = 4.5$, $\gamma = 20°$ (first figure) and $\mathrm{Fr}_1 = 7$, $\gamma = 40°$ (second figure), looking up into the streams along the deflecting dam. The bottom photograph shows a close-up of the second photograph, looking onto the side of the deflecting dam. It can be observed that the flow runs higher up on the deflecting dam at the start of the dam and then falls back on itself and the shock widens and becomes thinner.

4.2 Results

The incoming flow speeds and depths along with the Froude numbers in the two experimental series are summarised in Table 2. The first front of the flows splashed up higher on the dams than the steady hydraulic jumps. All of the experimental sets involved stabilised hydraulic jumps ($4.5 < \mathrm{Fr}_1 < 9$) that are relatively free of wave action, apart from the experiments on the $3°$ slope where the hydraulic jump is on the boundary of being a stabilised jump and might be categorised as a transitional jump with pulsating action (Hager, 1992). The Reynolds number is defined by $\mathrm{Re} = \rho u h / \mu$, where ρ is density and μ is viscosity. In the experiments, we find that Re is sufficiently large that viscous effects may be neglected.

The run-up profiles along the dams are plotted in Figure 19. The flow depth along the dams was found to be nearly constant, for dams at $\gamma \leq 20°$. For dams at the largest deflecting angles, $\gamma > 20°$, there was a zone at the beginning of the dams with higher run-up and overturning of the flow. The flow ran up, reached a maximum height and fell back upon the oncoming stream in a rotating motion. The flow depth in front of the dams was approximately constant further along the dams.

A possible explanation for the higher run-up and overturning of the flow at the beginning of the dams lies in the finite width of the highly turbulent transition zone. The width of the transition zone is denoted by Δl in Figure 20. The higher run-up occurs when the transition zone intersects with the beginning of the dams. The turbulence in the transition zone pushes the water higher up on the dams than the depth of the hydraulic jump along the dams. The region along the dam where the dam and the transition zone intersect will be referred to as the 'adjustment region'. The length of the adjustment region should increase with firstly smaller shock angles and secondly a wider transition zone. Figures 7 (a) and (b) show that the shock angle decreases with increasing Froude number, and for Froude numbers above 5 the shock angle is relatively independent of the deflecting angle. There should therefore be an increase in the length of the adjustment region with higher Froude number flows. Furthermore, studies of hydraulic jumps show that the transition zone widens as the shock height increases for Froude

Series	ξ [°]	u_1 [m s^{-1}]	h_1 [m]	Fr_1	Re
I	3	1.05 ± 0.05	0.00575 ± 0.00025	4.4 ± 0.3	6100
	6	1.25 ± 0.08	0.00475 ± 0.00025	5.8 ± 0.5	6000
	9	1.4 ± 0.1	0.00425 ± 0.00025	7.0 ± 0.8	6100
II	3	0.95 ± 0.05	0.0055 ± 0.0005	4.1 ± 0.4	5200
	6	1.18 ± 0.07	0.0045 ± 0.0005	5.6 ± 0.7	5300
	9	1.25 ± 0.08	0.004 ± 0.0005	6.4 ± 0.8	5000

Table 2: A description of the steady stream of the incoming flow for the two experimental series. Series I was used to measure the depth profile along the dam and series II to measure the shock angle.
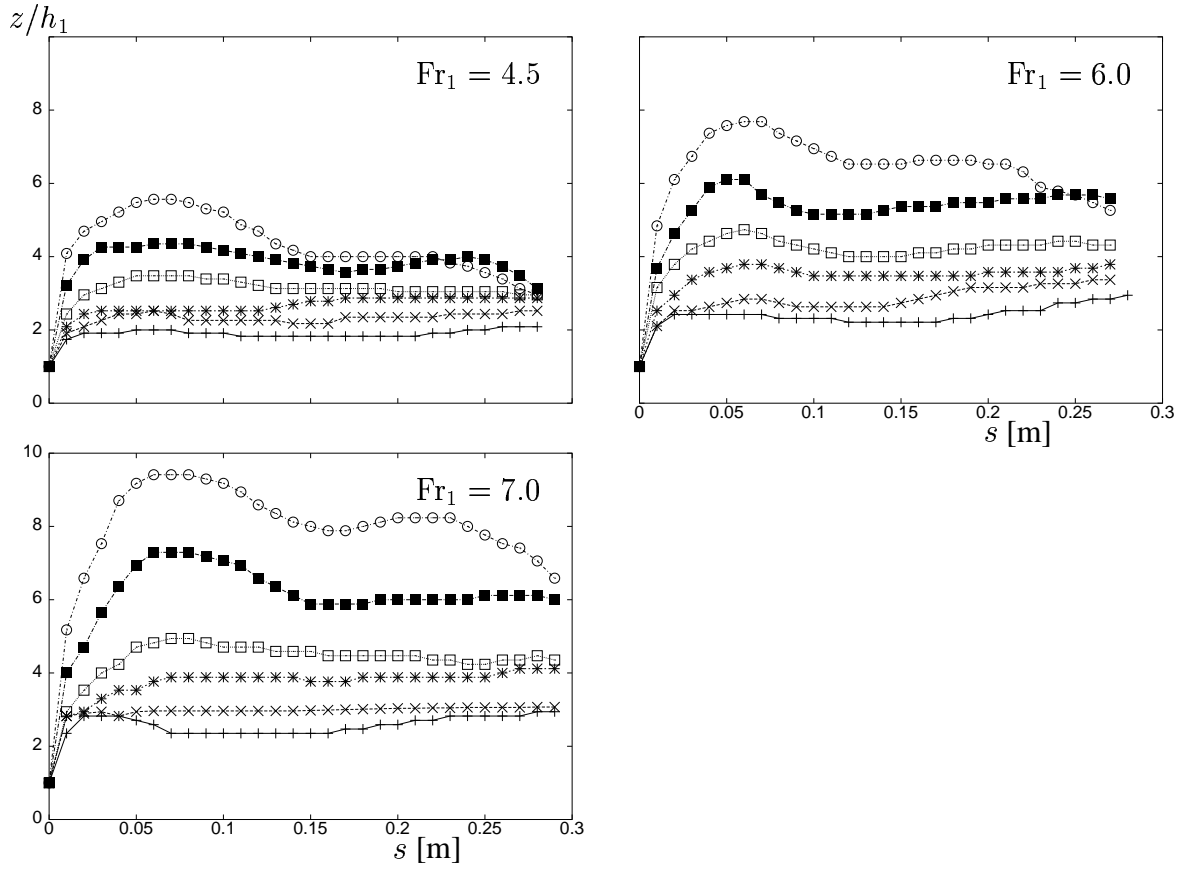
Figure 19: Non-dimensional run-up profiles along the deflecting dams of steady water at different Froude numbers. Each curve shows the steady shock height at a fixed deflecting angle. The deflecting angles tested were: $\gamma = 5\,°$, $10°$, $15°$, $20°$, $30°$ and $40°$. The shallowest profile on each graph corresponds to the $5°$ deflection and the deepest to the $40\,°$ deflection.

numbers up to around 7. (For $1 < \mathrm{Fr}_1 < 7$, $4 < \Delta l/h_2 < 6$, see for example (Gerhart *et al.*, 1993).) Figures 7 (c) and (d) show that the shock height increases with increasing deflecting angles for flows at fixed Froude numbers. The adjustment region should therefore also lengthen with wider deflecting angles. The shock height furthermore increases with higher Froude numbers for fixed deflecting angles, see Figure 19. That enhances the lengthening of the adjustment region for higher Froude number flows.

An increase in the length of the adjustment region with higher Froude number flows is not obvious from the run-up profiles in Figure 19 due to the narrow range of the Froude numbers. The transition zone in the experiments was observed to widen as a function of the deflecting angle (and consequently as a function of the flow depth of the hydraulic jump) from being just under $0.01\,\mathrm{m}$ for $\gamma = 5°$ to about $0.03\,\mathrm{m}$ for $\gamma = 40°$. A longer adjustment region for the larger deflecting angles is observable from the run-up profiles in Figure 19 due to this effect.
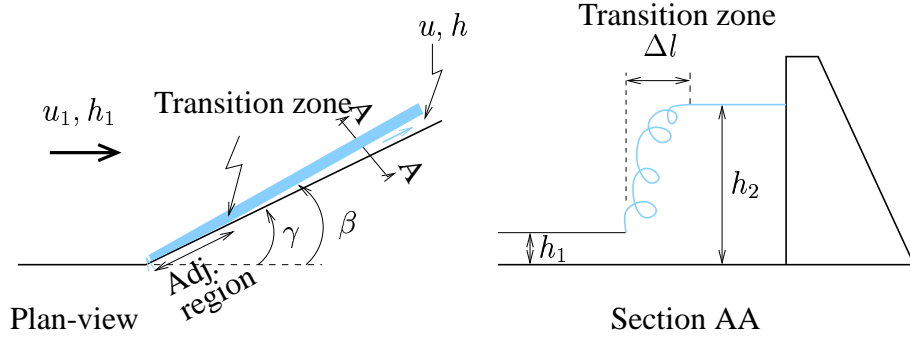
31

Figure 20: Schematic diagram of the adjustment region along a deflecting dam, caused by the intersection of the turbulent transitions zone with the deflecting dam.

The run-up at the beginning of the dams is observed to increase with increasing deflecting angles. That may be caused by the increase in the velocity component of the approaching flow normal to the dams, $u \sin \gamma$, since the pressure distribution in the turbulent adjustment region is far from being hydrostatic and the flow may follow ballistic trajectories along the side of the dam in this region.

We now compare the experimental results with the predictions of the steady-state shock theory in some detail. The system of equations (12), (13) and (14) was solved numerically for the shock depth, h_2, speed, u_2, and angle, β, for a given incoming flow depth, h_1, speed, u_1, and deflecting angle, γ. The shock angle relative to the dam, $\beta - \gamma$, is plotted in Figure 21 as a function of the deflecting angle. There is good agreement between the experimental results and the theory for the three experimental series. The predicted shock height is plotted as a straight line on Figures 22, 23 and 24 along with the observed run-up profile. The agreement is fairly good apart from the observed higher run-up at the beginning of the dams.

We conclude that the hydraulic jumps on shallow slopes are well described by the shallow-water jump conditions where constant flow states are assumed on both sides of the hydraulic jump. There is, however, a region close to the beginning of the dams where the flow runs higher up on the dams than the theory predicts, due to turbulence in the transition zone. This adjustment region lengthens, and the flow depth in front of the dams in the adjustment region increases relative to the surface of the constant hydraulic jump further down stream, with higher Froude number flows and larger deflecting angles.
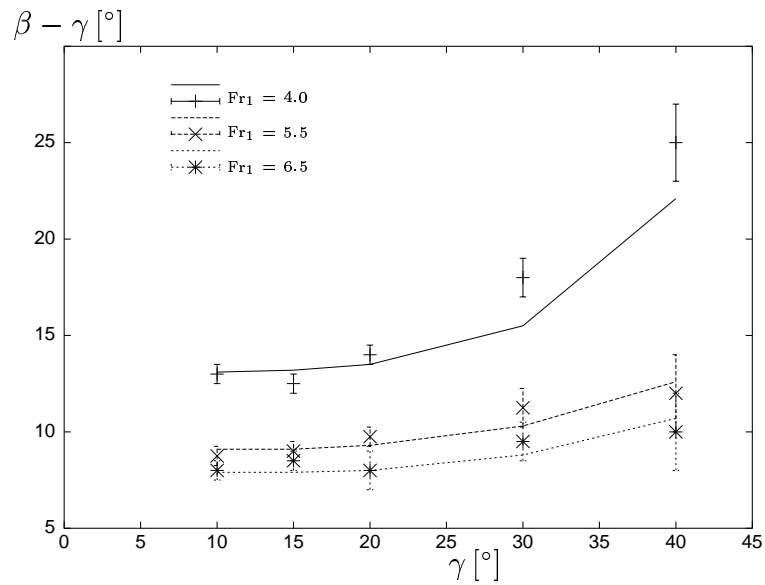
Figure 21: The shock angle relative to the dam plotted as a function of the deflecting angle for the three different Froude numbers. The lines show the theoretical predictions and the points are the experimental results.
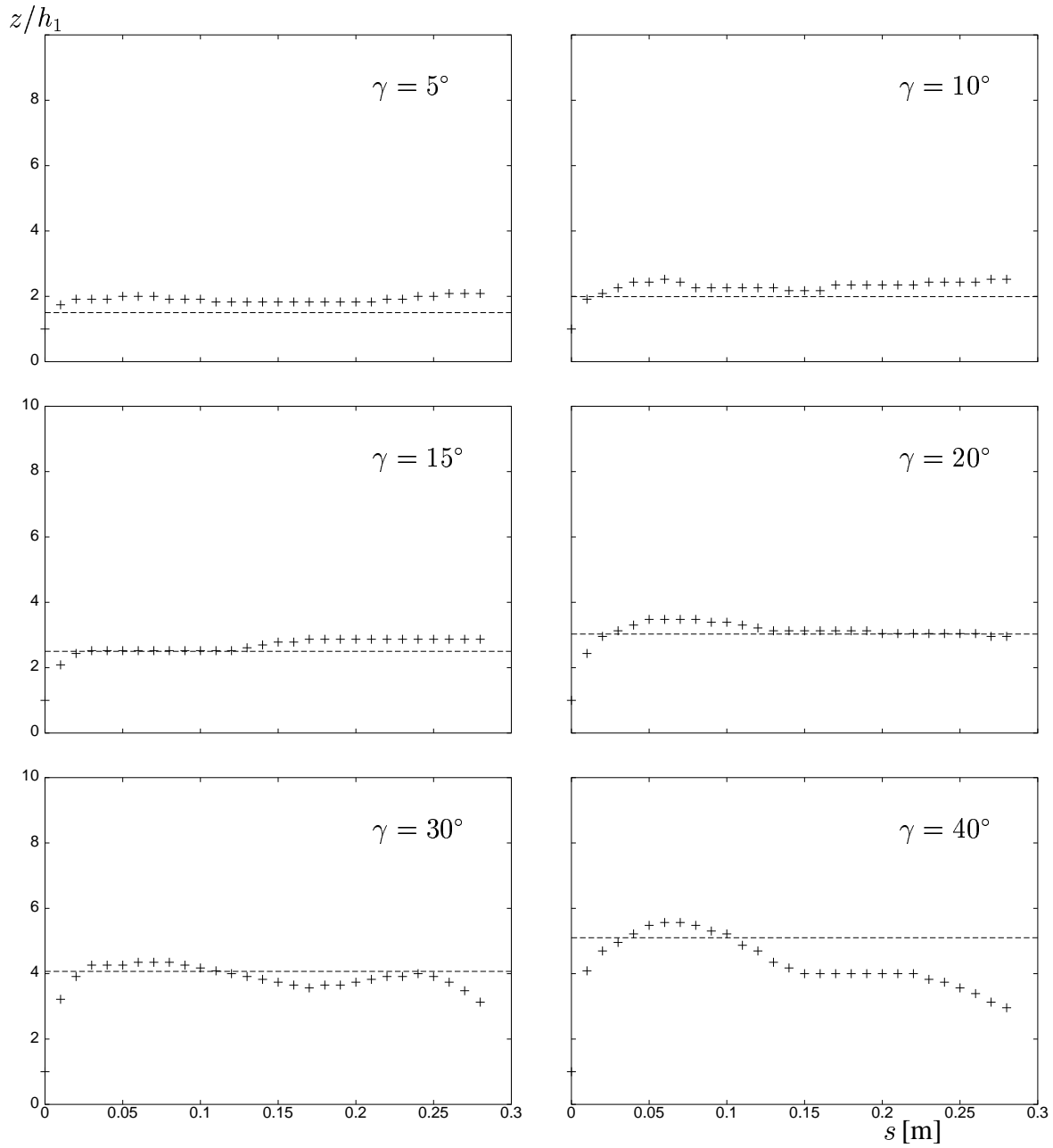
Figure 22: Non-dimensional run-up profiles for water flow at $Fr_1 = 4.5$. Each graph is a plot of the observed depth profile along the deflecting dam, non-dimensionalised with the depth of the incoming stream at a fixed deflecting angle, γ (+). The theoretical non-dimensional shock height, h_2/h_1, is shown with a dashed line.
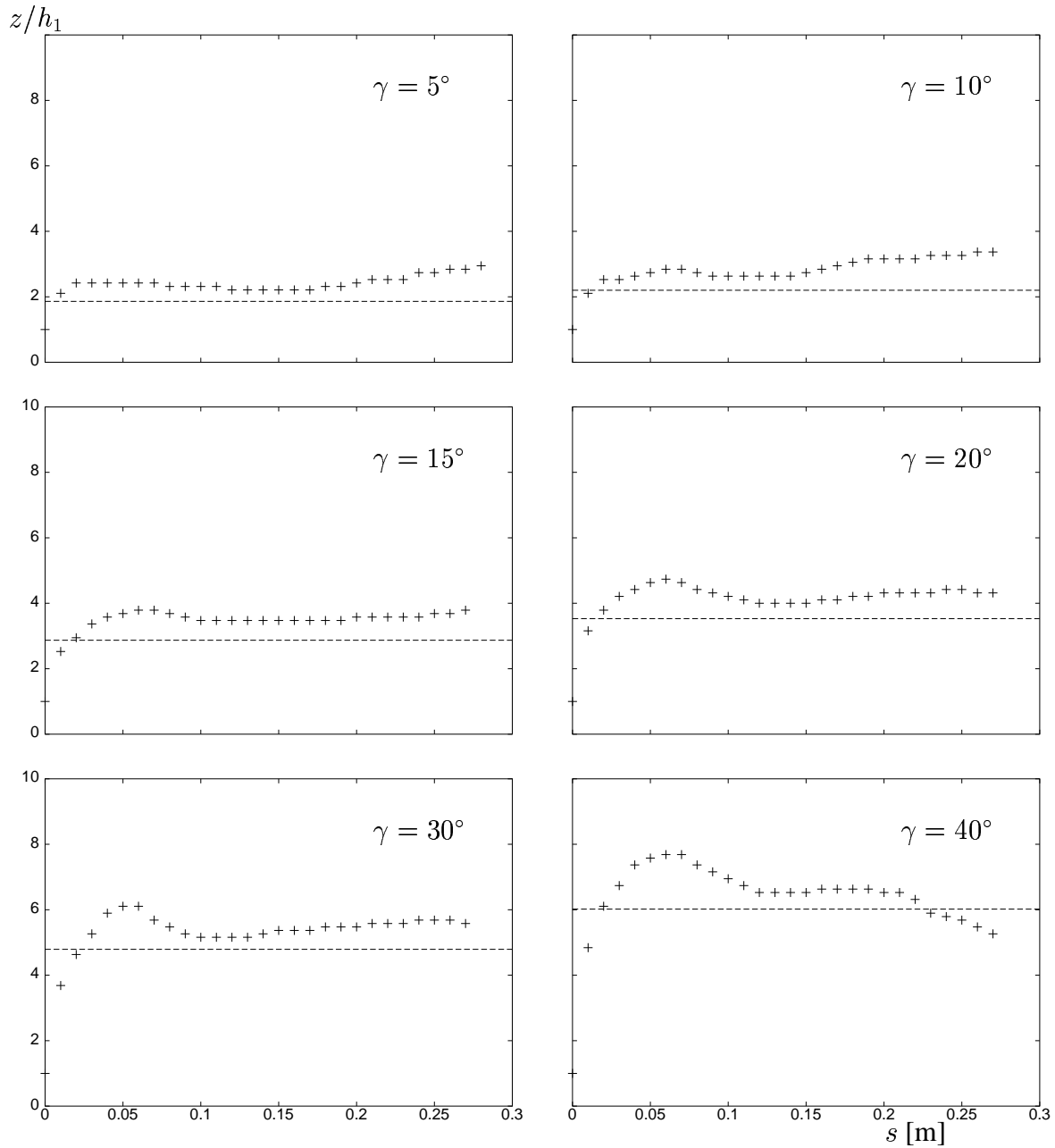
Figure 23: Non-dimensional run-up profiles for water flow at $Fr_1 = 6.0$. Each graph is a plot of the observed depth profile along the deflecting dam, non-dimensionalised with the depth of the incoming stream, for a fixed deflecting angle, γ (+). The theoretical non-dimensional shock height, h_2/h_1, is shown as a dashed line.
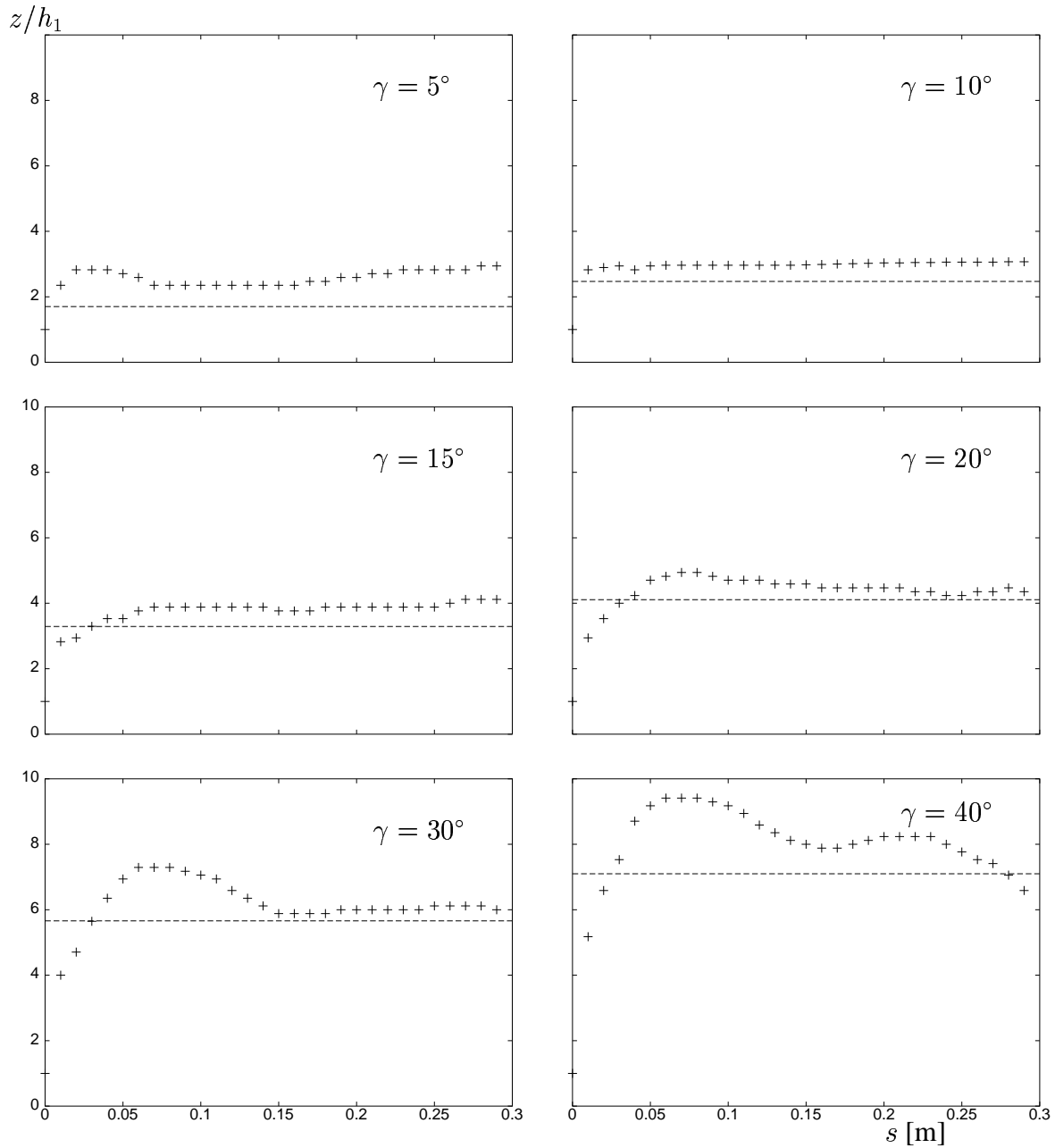
35

Figure 24: Non-dimensional run-up profiles for water flow at $\mathrm{Fr}_1 = 7.0$. Each graph is a plot of the observed depth profile along the deflecting dam, non-dimensionalised with the depth of the incoming stream, for a fixed deflecting angle, γ (+). The theoretical non-dimensional shock height, h_2/h_1, is shown as a dashed line.

5 Laboratory experiments of steady granular flows interacting with deflecting and catching dams

A series of experiments at three different Froude numbers was designed to study the formation of a steady, oblique, granular shock along a deflecting dam, positioned on a sloping chute. The objective of the experiments was to maintain a steady flow for a few seconds in order to link the granular jumps on steep slopes, described in § 3, to the hydraulic jumps on shallow slopes, described in § 4. The effect that tilting of the upstream dam faces had on the oblique shocks was also investigated. The formation of a granular jump upstream of a catching dam was then explored and the height of the catching dam at which a bore could no longer be maintained upstream of the dam was determined.

5.1 Experimental setup and design

Figure 25: A photograph of the steady, granular experimental setup.

The same setup and the same particles were used as in the short granular experiments described in § 3.1, but with the channel narrowed by 0.1 m, to 0.225 m. The release mechanism was adjusted so that it was possible to control the depth of the flow out of the hopper. As before, the flow was released by abruptly opening a lock gate, see Figure 25.

The experiments within each series were conducted during a 12 hour period to minimise the effect of changes of the humidity in the laboratory on the ballotini beads. The flow speed and depth were measured at the start and end of each experimental set. The flow speed was measured by tracking tracer particles that were thrown into the flow and the flow depth was measured using an optical depth sensor (ODS96) that uses infrared light to measure the distance to a surface.

The deflecting dam experiments were conducted at three different Froude numbers: $5, 12$ and 14, overlapping the values in the previous experiments with water and granular flows, and for five different deflecting angles: $\gamma = 8°, 15°, 24°, 32°$ and $44°$. The dams had an upstream face perpendicular to the experimental chute, $\alpha = 90°$, where α is the angle between the upstream dam face and the chute. The dams were 0.5 m long and covered different proportions of the flow path, l/L, see Figure 8 (b) for definitions. For $\gamma = 8°, 15°$ and $24°, l/L < 1$, but for $\gamma = 32°, l/L = 1.1$ and for $\gamma = 44°, l/L = 1.5$, which means that the dams extended out of the flow-path for the two largest deflecting angles.

The flow depth along the dams and the shock angles at the dams were measured from video footage of the experiments. The flow speed was measured inside the shock, along the deflecting dam, for $\gamma = 24$ °, by tracking tracer particles that were thrown into the flow. The effect of tilting the sidewalls of the dams was examined for $Fr_1 = 12$, $\gamma = 24°$ and $\alpha = 90°$, $75°, 60°$ and $45°$, again by measuring the steady shock angle and flow depth along the dam for each value of α.

Catching dam experiments were conducted for flows at $Fr_1 = 12$ and 14. The dams had an upstream face perpendicular to the experimental chute. The height of the dams was systematically lowered and the speed of the bore travelling upstream was measured along with the depth of the bore and the depth of the flow over-topping the dam when overflow occurred. The effect of tilting the upstream face of the dams to $\alpha = 60°$ was also explored.

5.2   Results: Deflecting dams

The characteristics of the steady stream are given in Table 3. The flow reached a steady, uniform state (constant flow speed and depth) very quickly (within the first tens of centimetres from the release) on the steep section of the experimental chute. The steady stream hit the deflecting dam approximately 2 m further down and a stationary oblique shock was formed within a fraction of a second of the initial impact, see Figure 26. The dilute first front of the flow splashed up to a similar height on the dams as the shock.

The run-up profiles along the dams are plotted in Figure 27 for the three different Froude number flows. The oblique shocks were stationary for all but the largest deflecting angles. The dams for the $32°$ and $44°$ deflections extended out of the flow path of the avalanches leading to the slowing down of the current along the end of the dams and the subsequent pile up of material in front of the dams. This was observed for $Fr_1 = 5$ with $\gamma = 32°$ and $44°$ and also for $Fr_1 = 12$ and 14 with $\gamma = 44°$. The plotted profiles of the unsteady flows are those that were observed before the material started to pile up in front of the dams.
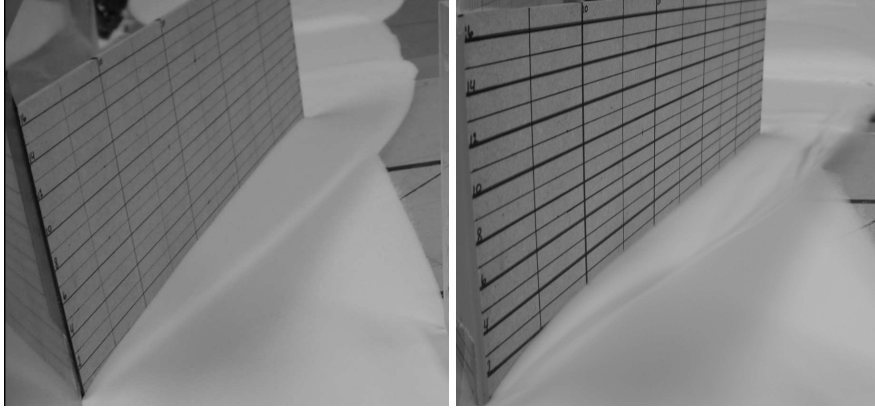
Figure 26: Photographs of oblique, granular shocks for $\gamma = 24°$ for two different Froude numbers, $Fr_1 = 5$ and 12, on slopes inclined at $\xi = 26°$ and 30°, looking downstream onto the deflecting dams. The shock is narrower on the photograph to the right ($Fr_1 = 12$) and the flow flips over and falls back on the oncoming stream at the beginning of the dam.

ξ [°]	u_1 [m s^{-1}]	h_1 [m]	Fr_1
26.5 ± 0.5	0.7 ± 0.01	0.0020 ± 0.0002	5
30.3 ± 0.5	1.85 ± 0.07	0.0027 ± 0.0002	12
30.3 ± 0.5	1.52 ± 0.05	0.0013 ± 0.0002	14

Table 3: A description of the steady stream of granular flow for the three different experimental setups.

If these unsteady profiles are not considered, the run-up profiles along the dams show an approximately constant depth along the dams. The profiles follow the same trend as previously observed for the water and granular flows; larger Froude numbers and deflecting angles lead to higher run-up on the dams.

The turbulent transition zone intersected with the upper most part of deflecting dams in the water experiments and the flow ran higher up on the dams in this region relative to the hydraulic jump further downstream. This effect is less profound in these granular experiments since higher run-up on the dams is not observable from the run-up profiles. The flow was, nevertheless, observed to turn over and fall back on itself at the start of the deflecting dams for the the higher Froude number flows, $Fr_1 = 12$ and 14, see Figure 26. The transition zone was observed to be much thinner than in the water experiments (less than 0.01 m wide for all of the deflecting angles).

The experimental results can be compared with the shallow-water jump conditions. Equations (12), (13) and (14) were solved numerically for the shock depth, speed and angle: h_2, u_2 and β, for a given incoming flow depth, speed and deflecting angle: h_1, u_1 and γ. The shock
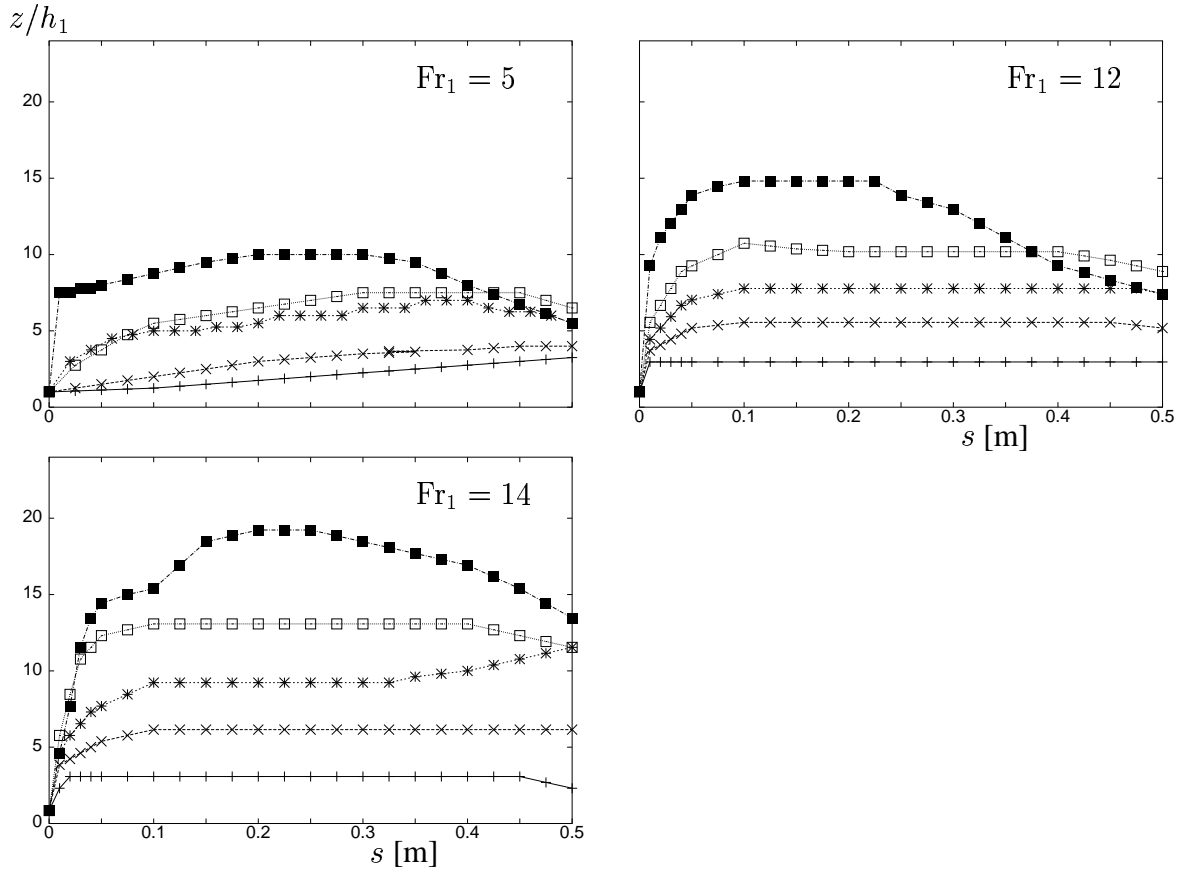
Figure 27: Non-dimensional run-up profiles along the deflecting dams for steady, granular flow at three different Froude numbers, $Fr_1 = 5, 12, 14$. Each curve shows the steady shock height for a fixed deflecting angle, the different curves belong to different deflecting angles; $8°$, $15°$, $24°$, $32°$ and $44°$. The shallowest profile on each graph corresponds to the $8°$ deflection and the deepest to the $44°$ deflection. The profiles for $Fr_1 = 5$ with $\gamma = 32°$ and $44°$ and for $Fr_1 = 12$ and 14 with $\gamma = 44°$ were unsteady.

angle is plotted as a function of the deflecting angle in Figure 28. The shallow-water theory accurately predicts the experimental results for all three Froude numbers. The observed depth profiles along the dams are plotted in Figures 29, 30, 31, and show good agreement with the predicted shock height after the short distance along the dams that it takes the flow to reach the depth of the hydraulic jump. The depth profiles for the $Fr_1 = 5$ show a slight increase in the flow depth along the dams while there is no increase in the flow depth for the higher Froude number flows.

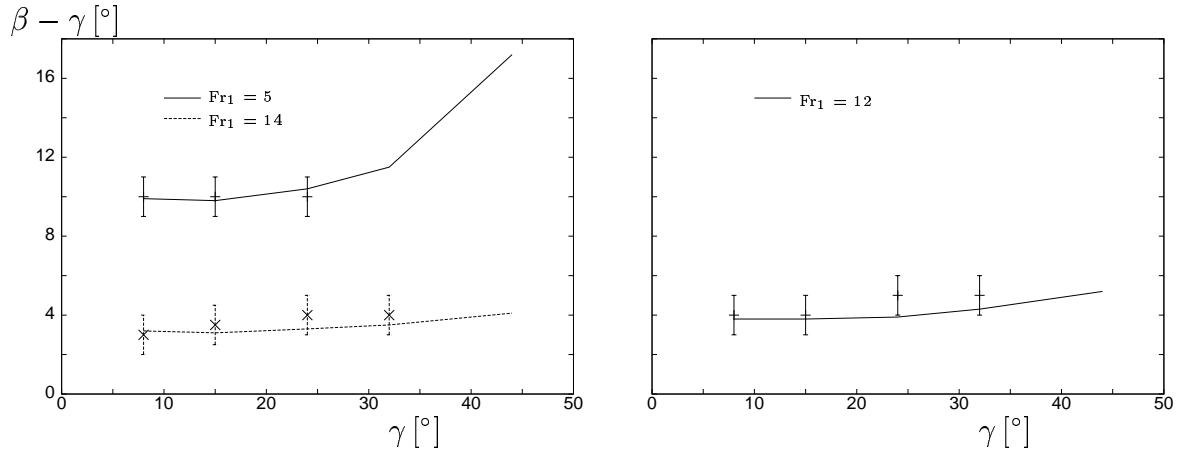The effect of tilting the sidewalls of the dams between $\alpha = 45°$ and $\alpha = 90°$ for $Fr_1 = 12$

Figure 28: The shock angle relative to the dam, $\beta - \gamma$, plotted as a function of the deflecting angle for the three different Froude numbers. The lines show the theoretical predictions and the points are the experimental results. The shocks were unsteady for $Fr_1 = 5$ and $\gamma = 32°$ and $44°$; $Fr_1 = 12$ and 14 and $\gamma = 44°$, so that no shock angle was observed.

did not affect the shock formation. The shock angle and the depth, measured normal to the chute, remained the same as for a deflecting dam normal to the chute, $\alpha = 90$ °. The area per unit width of the dam over which the normal pressure acts is $h_2/\sin\alpha$, where h_2 is the flow depth at the dam, measured normal to the chute. The total normal force on a unit width of the dam thus becomes $\rho g^\star h_2^2/(2\sin\alpha)$ and increases by a factor of $\sqrt{2}$ for dams at $\alpha = 45°$ compared with dams at $\alpha = 90°$. The Coulomb friction force on the dams is proportional to the normal force on the dams, and thus increases by tilting the dams. If Coulomb friction affects the run-up onto the dams, there should be a visible difference in the run-up profiles on the dams for dams tilted at different angles. This does, however, not seem to be the case in these high Froude number experiments.

We conclude that shallow-water jump conditions that assume constant flow states on both sides of the jump can be used to describe granular jumps along deflecting dams on non-accelerative slopes (the flows were steady). Coulomb friction at the side of the dams is not observed to affect the characteristics of the shock for the high Froude number flows, $Fr_1 = 12$, that were studied.
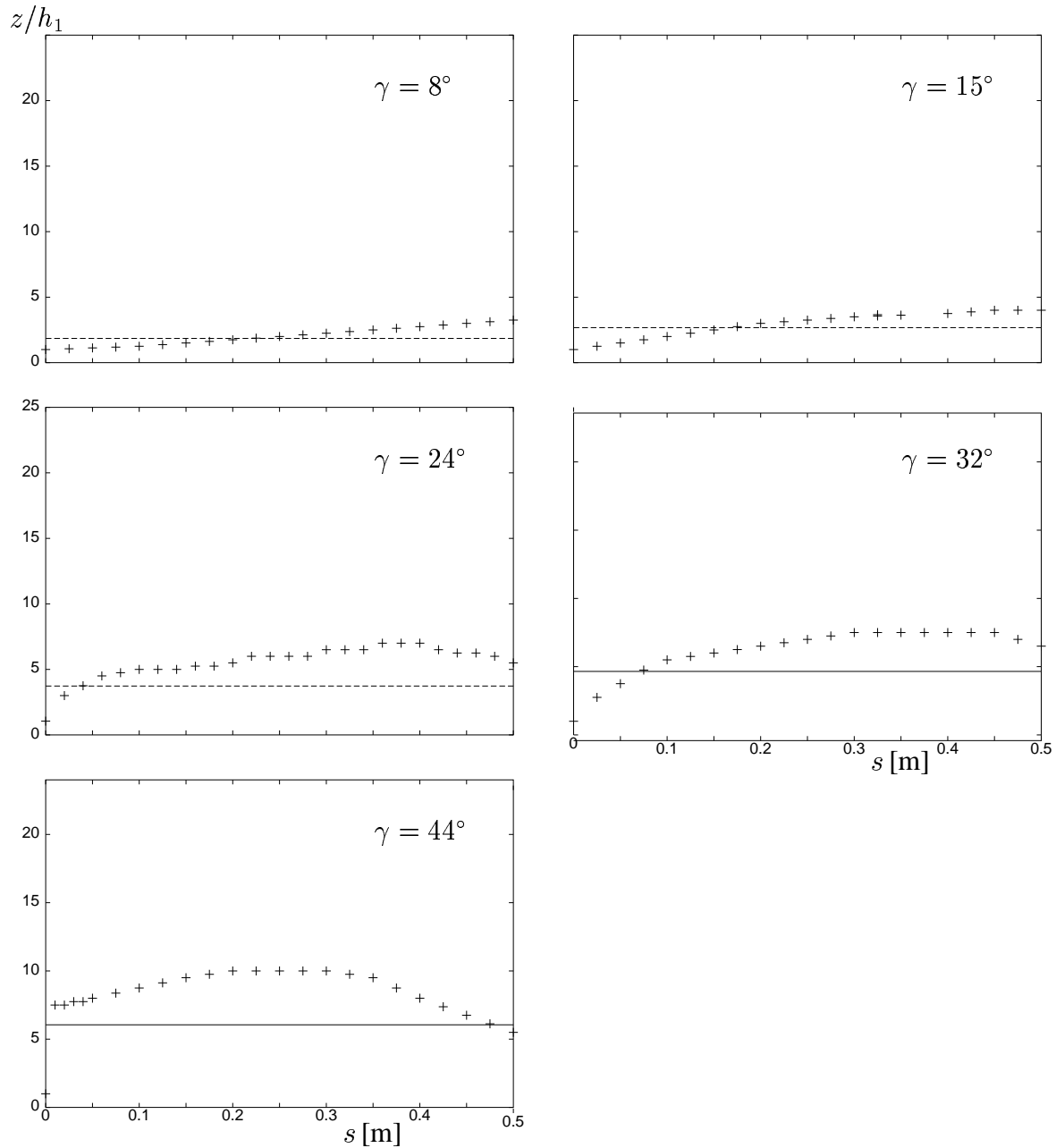
Figure 29: Non-dimensional run-up profiles for granular flow at $\mathrm{Fr}_1 = 5$. Each graph is a plot of the observed depth profile along the deflecting dam, non-dimensionalised with the depth of the approaching stream, for a fixed deflecting angle, γ (+). The theoretical non-dimensional shock height, h_2/h_1, is shown as a dashed line. The shocks were unsteady for $\gamma = 32°$ and $44°$ where the shock height is drawn as a solid lines.
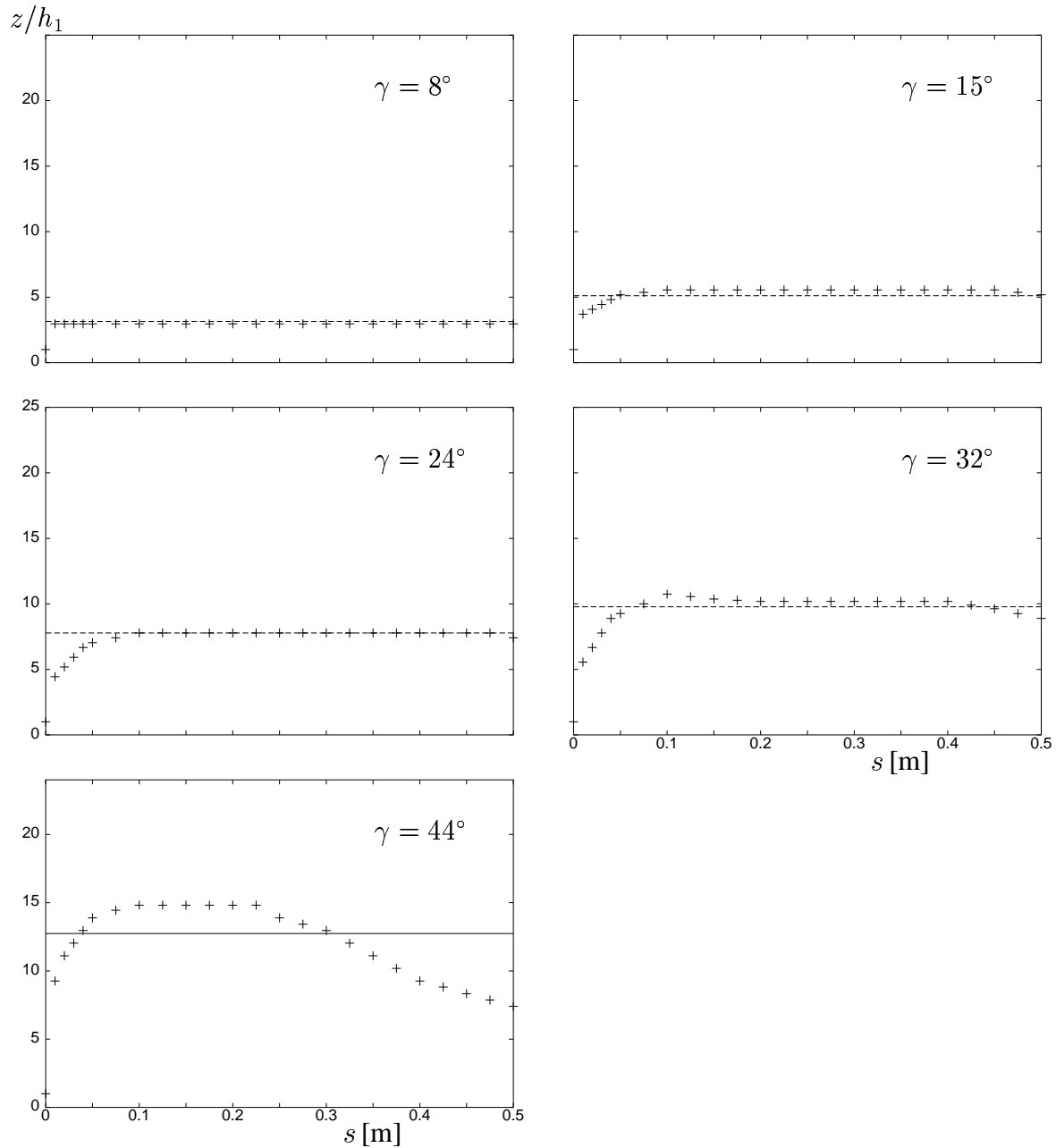
Figure 30: Non-dimensional run-up profiles for granular flow at $\mathrm{Fr}_1 = 12$. Each graph is a plot of the observed depth profile along the deflecting dam, non-dimensionalised with the depth of the approaching stream, for a fixed deflecting angle, γ (+). The theoretical non-dimensional shock height, h_2/h_1, is shown as a dashed line. The shock was unsteady for $\gamma = 44°$ where the shock height is drawn as a solid line.

43

Figure 31: Non-dimensional run-up profiles for granular flow at $\mathrm{Fr}_1 = 14$. Each graph is a plot of the observed depth profile along the deflecting dam, non-dimensionalised with the depth of the approaching stream, for a fixed deflecting angle, γ (+). The theoretical non-dimensional shock height, h_2/h_1, is shown as a dashed line. The shock was unsteady for $\gamma = 44°$ where the shock height is drawn as a solid line.
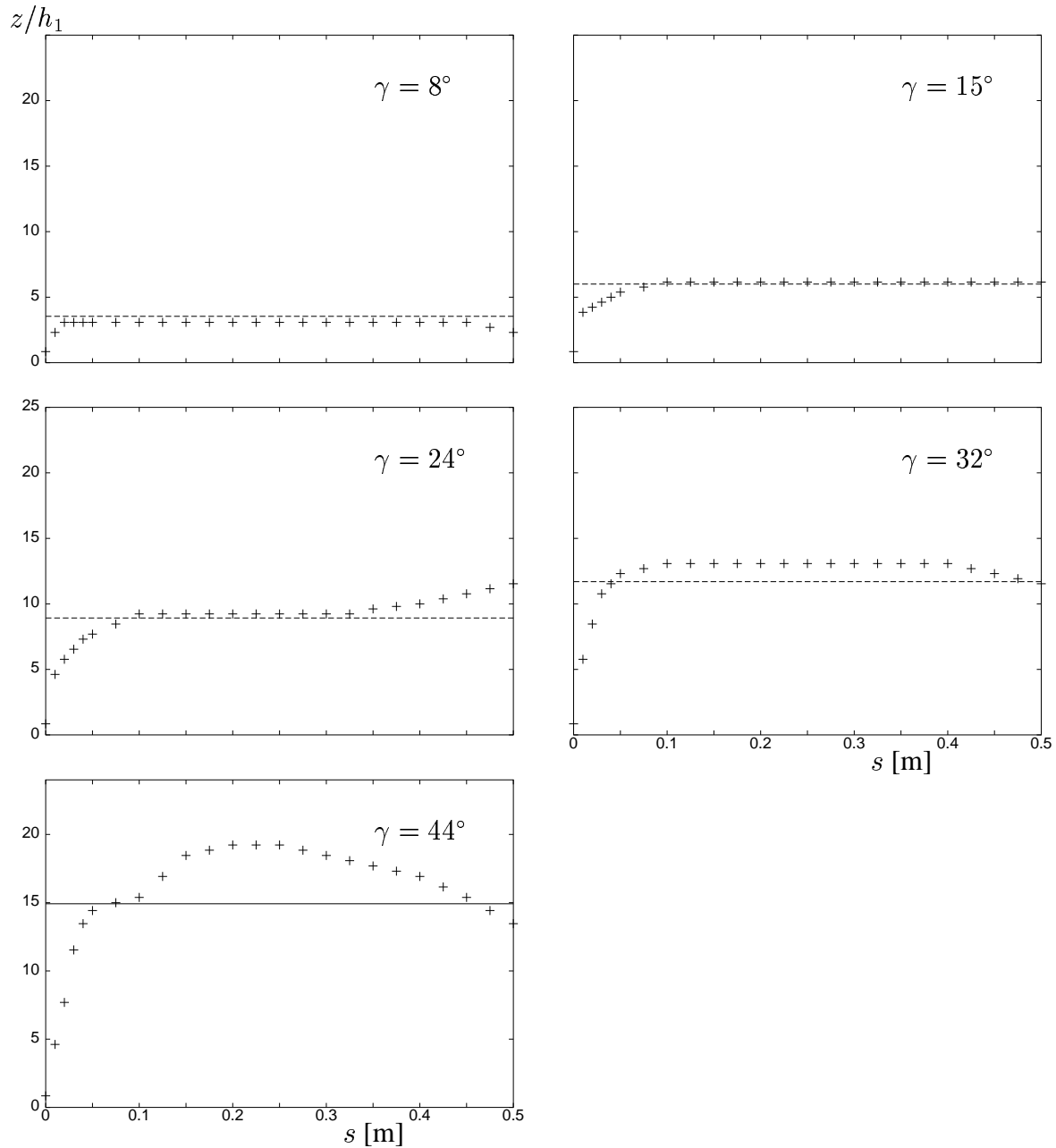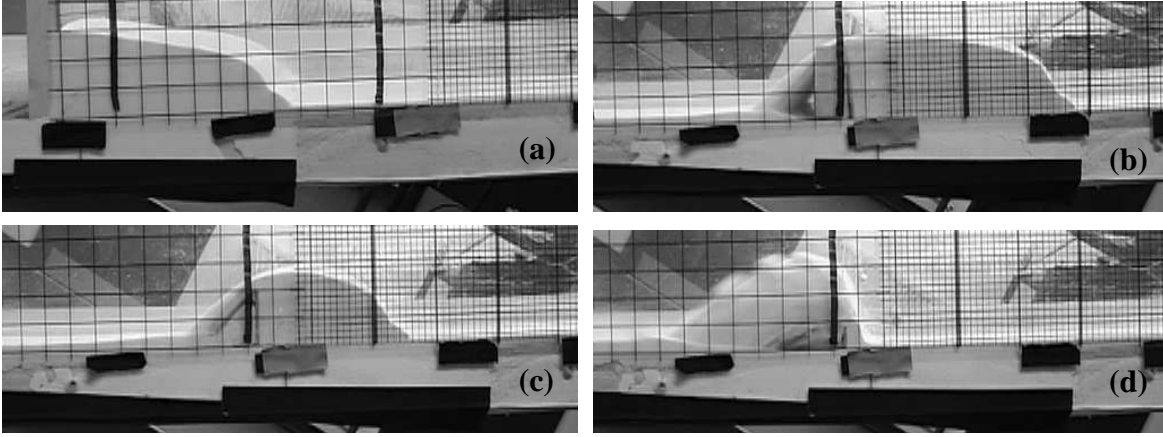
44

5.3   Results: Catching dams

Figure 32: Photographs of granular flow at $\mathrm{Fr}_1 = 12$, travelling from right to left down a $30°$ incline and interacting with (a) a high catching dam (on the left) and forming a bore that travels upstream; (b) a lower catching dam, $H/h_1 = 18$, with some of the flow over-topping the dam and a stationary bore upstream of the dam; (c) an even lower catching dam, $H/h_1 = 15$, where the stationary bore is closer to the dam; (d) a lower still catching dam, $H/h_1 = 11.5$, where all of the flow over-tops the dam. Note that the incoming flow is only 0.002 m thick and hardly visible on the photographs. The dimensions of the larger grid-cells are (0.02×0.02) m.

Experiments with flows at Froude numbers 12 and 14 revealed that granular bores travelling upstream were formed in front of catching dams (see Figure 32). The dilute first front of the flow splashed higher up on the dams than the granular jump. The angle of repose of the granular material (ballotini beads) was smaller than the slope of the chute, $\phi = 21° < \xi = 30°$. The free surface of the stationary material in front of the dam (downstream of the shock) was intermittently levelled out to the angle of repose of the ballotini beads by thin avalanches on the free surface, propagating from the start of the bore and down to the catching dam. The bore slowed down during the upstream propagation, as more material avalanched down to the dam in order to level out the lengthening free surface of the bore. An upstream propagating bore was still present in front of the dam, when the height of the dam was lowered, so that some of the flow over-topped the dam. The bore propagated upstream until the mass flux over the bore balanced the mass flux over the dam at which point the bore stopped. The distance travelled upstream by the bore shortened when the dam was lowered, until a granular jump upstream of the dam disappeared and all of the flow was launched over the dam.

The scenario where a shock is formed upstream of a catching dam and the dam is high enough so that no part of the flow over-tops is described by equations (3) and (6) when $\phi < \xi$.
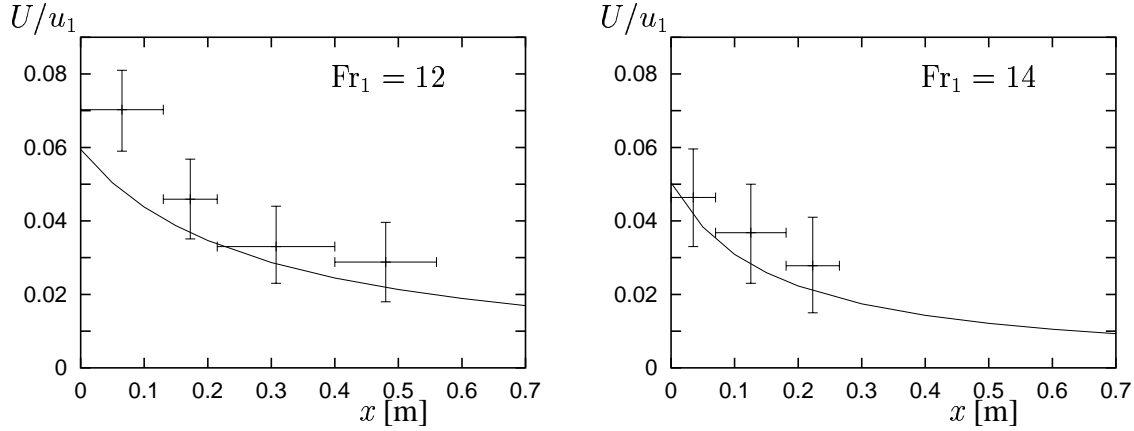
45

Figure 33: The borespeed non-dimensionalised with the speed of the approaching flow, U/u_1, plotted as a function of the distance travelled upstream by the bore, x, for $\mathrm{Fr}_1 = 12$ and 14. The theoretical prediction for material with $\phi \geq \xi$ is plotted as a straight line. The observed bore speed for $\xi - \phi = 9°$ is averaged over the distance indicated by the x-error bars (+).

The shock height and the time dependent position of the bore front were accurately predicted by the theory by using the same density on both sides of the bore, $\rho_2 = \rho_1$, see Figure 33. Gray *et al.* (2003) have conducted similar catching dam experiments using material with a larger internal friction angle than the angle of the slope on which their flows take place. They find that the system of equations referred to above predicts the speed and the depth of the upstream propagating bore. (Gray *et al.* furthermore conduct their experiments at slope angles that balance the basal friction angle of the flow so that gravity does not affect the conservation of momentum flux over the bore, but they do not comment on the results when gravity is not matched by Coulomb friction.)

When the catching dam was lower than the shock height, some of the flow over-topped the dam. The setup is described by the system of equations (7), (8), (10) and (11), for $\phi < \xi$ and a constant flow state downstream of the shock. For a given approaching flow depth and speed: h_1, u_1, the bore height, bore speed, overflow height and overflow speed: h_2, U, h_3, u_3, can be determined.

Experiments with flows at $\mathrm{Fr}_1 = 12$ showed that the bores travelled a certain distance upstream where they then stopped. The flow was in a constant flow state upstream of the shock and may to some approximation be regarded as being in a constant flow state downstream of the shock. The shock depth and overflow depth, h_2 and h_3, were well predicted by the theory. The theory also predicted the position of the stationary bore, see Figure 34. The dam height leading to no shock formation upstream of the dam was furthermore accurately predicted by the theory, *i.e.* the dam height resulting in a computed negative bore speed. The ratio between the dam height leading to no shock formation and the initial shock height for no overflow was found to be $H/h_2 \approx 0.65$. Equation (4) with $\rho_2/\rho_1 = 1$ can be used to approximate the dam
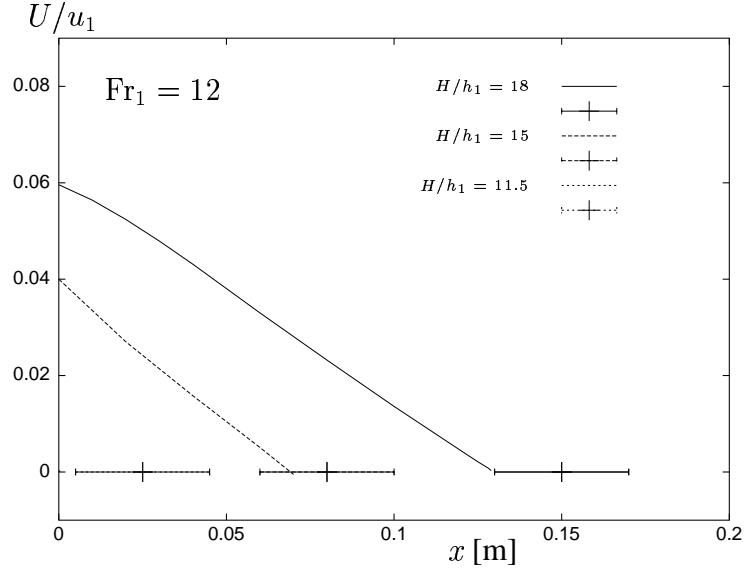
Figure 34: The theoretically predicted bore speed non-dimensionalised with the speed of the approaching flow, U/u_1, plotted as a function of the distance travelled upstream by the bore, x, for different dam heights, H. The speed $U = 0$ indicates that the bore has stopped and the experimental observations of the stopping position of the bore are plotted for the three different dam heights (+). For $H/h_1 = 11.5$, the theory predicts that the bore would only travel half a millimetre upstream. The theoretical line is therefore not visible on the plot.

height corresponding to no shock formation as a function of the depth of the incoming flow and the Froude number.

$$H \approx 0.65\, h_2 \approx 0.65\sqrt{2}\mathrm{Fr}_1 h_1 \approx 11 h_1.$$

The effect of tilting the upstream face of the catching dam had no effect on the shock height and bore propagation. It was observed, however, in the experiments that the first front splashed up higher on the dams than the immediately following shock and the angle at which the first front took off from the top of the dams coincided with the angle of the upstream dam face.

We conclude that the shallow-water framework gives accurate predictions of the granular jumps, while the splash-up of the dilute and compressible first front of the flow onto the dams remains a subject of future work.

47

6 Discussion

The experimental study has considered steady, supercritical flow of water and dry, granular material interacting with dams. The flows were at different Froude numbers, were of different physical scales (different flow depth and speed) and took place on steep and shallow slopes. The experiments revealed that the dry, dense, granular free surface flows scale with the internal Froude number of the flow as do flows of water. Features such as shocks were observed upstream of the dams in the granular flows as well as in the water flows. A better agreement between theory and experiments was obtained for the granular flows if the pressure was taken to be isotropic and hydrostatic, instead of linking the longitudinal and normal stresses through an earth pressure coefficient.

Stationary, oblique shocks were formed in the interaction of the flows with deflecting dams. They were well described by incompressible, shallow-layer shock theory, derived on a horizontal plane, assuming constant flow states on both sides of the shock. Less intense wave action and turbulence were observed in the granular flows than in the water, presumably owing to dissipation in inelastic collisions between grains and this may account for a sharper transition zone in the granular material. The structure of the granular jumps was not observed to depend on the Froude number of the approaching flow for the Froude number range that was studied, $5 < \mathrm{Fr}_1 < 14$, as is the case in hydraulic jumps. Higher run-up than the jump conditions predicted and turn-over of the flow was observed close to the upstream end of the deflecting dams for the higher Froude number granular flows and for water flow at the largest deflecting angles and for all Froude numbers. This effect was more obvious for the water because of a more turbulent and wider transition zone.

A travelling bore was formed upstream of the catching dams when none of the flow over-topped the dams. For lower dams with some overflow, a shock could still be observed. As the height of the dams was gradually lowered, the bores stopped closer to the dams and finally the flow shot ballistically over the dams in a supercritical flow state and a shock did not form upstream of the dams. The granular jumps were well described by the shallow-water jump conditions. The internal friction angle of dry snow is suggested by Salm (1993) to be close to $25°$. In most cases avalanche protection dams will be positioned in the run-out zone of an avalanche path and not at angles steeper than $25°$. The theoretical consideration for $\phi \geq \xi$ would therefore in most cases be appropriate for the analysis of snow avalanches. The snow stopped by a catching dam may furthermore be more densely packed than the flowing avalanche leading to a density difference over the shock (mostly in the range $1 < \rho_2/\rho_1 < 3$) and a lower shock height at the dam than for an incompressible jump, such as a hydraulic jump.

Highly compressible flows with Mach numbers larger than one were not considered in the experiments (excluding the first front of the flows). There is a possibility that the dense core of some natural dry-snow avalanches is slightly supersonic (Briukhanov *et al.*, 1967) which may give rise to the formation of compression shocks in the interaction with dams. Such compression shocks have been observed experimentally in dilute granular flows (Rericha *et*

48

al., 2002).

The higher splash-up of the first front of the flows onto the catching dams is consistent with high pressures (impulse pressures) measured during the first few milliseconds of the impact of an avalanche with a catching dam (Bozhinskiy and Losev, 1998; Schaerer and Salway, 1980; Kotlyakov, *et al.*, 1977; and Salm, 1964) and also pressure records and observed splash-up of steep water waves on walls, see Peregrine (2003) for an overview.

The results presented here are a step towards a better understanding of the dynamics of dense granular flows, such as snow avalanches, that hit deflecting and catching dams. These results may be used to formulate new design criteria for such dams. They might also be useful for implementing deflection dynamics in numerical models that could be used to evaluate the effectiveness of dams as protection measures for settlements, communication lines and other properties and infrastructure. An important consideration in the application of our results to pratical design of protection dams is the question of the formation of the shock in the initial impact with the dam. In order for the shock to form, the flow must undergo a change in flow state from a supercritical flow to a subcritical flow as it passes over the dam. The presence of a shock is assumed in the derivation of the theoretical shock relations in section §2. The dam height needed for a hydraulic jump to occur in the first place will be larger than the theoretical bore height if the loss of energy across the granular jump is larger than the energy loss in the impact of the flow with the catching dam. This will, however, not be further discussed here.

7 Acknowledgements

References

Bozhinskiy, A. N. and Losev, K. S. (1998). The Fundamentals of Avalanche Science. *Mitt. Eidgenöss. Inst. Schnee- Lawinenforsch.*, 55:280 S.

Briukhanov, A. V., Grigorian, S. S., Miagkov, S. M., Plam, M. Y., Shurova, I. Y., Eglit, M. E., and Yakimov, Y. L. (1967). On some new approaches to the dynamics of snow avalanches. In *Physics of Snow and Ice*, volume 1, part 2, pages 1223–1241. Proc. of the Intl. Conf. on Low Temperature Science, Sapporo 1966, The Institute of Low Temperature Science, Hokkaido University, Sapporo Japan.

Chu, T., Hill, G., McClung, D. M., Ngu, R., and Sherkat, R. (1995). Experiments on granular flow to predict avalanche runup. *Canadian Geotechnical Journal*, 32:285–295.

Dias, F. and Christodoulides, P. (1991). Ideal jets falling under gravity. *Physics of Fluids A*, 3(7):1711–1717.

Eglit, M. E. (1983). Some mathematical models of snow avalanches. In Shahinpoor, M., editor, *"Advances in the Mechanics and the Flow of Granular Materials"*, volume 2, pages 577–588. Clausthal-Zellerfeld and Gulf Publishing Company.

Gerhart, P. M., Gross, R. J., and Hochstein, J. I. (1993). *Fundamentals of Fluid Mechanics*. Addison-Wesley, 2 edition.

Gray, J. M. N. T., Tai, Y.-C., and Noelle, S. (2003). Shock waves, dead-zones and particle-free regions in rapid granular free surface flows. *Journal of Fluid Mechanics*, 491:161–181.

Hager, W. H. (1992). *Energy Dissipators and Hydraulic Jump*. Kluwer Academic Publishers.

Hager, W. H. and Vischer, D. L. (1995). *Energy dissipators*. Balkema Publishers.

Hákonardóttir, K. M., Hogg, A. J., Batey, J., and Woods, A. W. (2003a). Flying avalanches. *Geophysical Research Letters*, in press.

Hákonardóttir, K. M., Hogg, A. J., Jóhannesson, T., and Tómasson, G. G. (2003b). A laboratory study of the retarding effect of braking mounds on snow avalanches. *Journal of Glaciology*, in press.

Hopfinger, E. J. (1983). Snow avalanche motion and related phenomena. *Ann. Rev. Fluid Mech.*, 15:47–76.

Irgens, F., Schieldrop, B., Harbitz, C. B., Domaas, U., and Opdahl, R. (1998). Simulations of dense-snow avalanches on deflecting dams. *Annals of Glaciology*, 26:265–271.

Issler, D. (2003). Experimental information on the dynamics of dry-snow avlanches. In Hutter, K. and Kirchner, N., editors, *Response of granular and porous materials under large and catastrophic deformations*, volume 11 of *Lecture notes in applied and computational mechanics*, pages 109–160. Springer (Berlin).

Jóhannesson, T. (2001). Run-up of two avalanches on the deflecting dams at Flateyri, north-western Iceland. *Annals of Glaciology*, 32:350–354.

Kotlyakov, V. M., Rzhevskiy, B. N., and Samoylov, V. A. (1977). The dynamics of avalanching in the Khibins. *Journal of Glaciology*, 19:431–439.

McClung, D. M. and Mears, A. I. (1995). Dry-flowing avlanche run-up and run-out. *Journal of Glaciology*, 41:359–372.

Peregrine, D. H. (2003). Water-wave impact on walls. *Annual Review of Fluid Mechanics*, 35:23–43.

Perla, R., Cheng, T. T., and McClung, D. M. (1980). A two-parameter model of snow-avalanche motion. *Journal of Glaciology*, 26:197–207.

Pouliquen, O. and Forterre, Y. (2002). Friction law for dense granular flows: application to the motion of a mass down a rough inclined plane. *Journal of Fluid Mechanics*, 453:133–151.

Rericha, E. C., Bizon, C., Shattuck, M. D., and Swinney, H. L. (2002). Shocks in Supersonic Sand. *Phys. Rev. Lett.*, 88(014302).

Salm, B. (1964). Anlage zur Untersuchung dynamischer Wirkungen von bewegtem Schnee. *ZAMP*, 15:357–375.

Salm, B. (1993). Flow, flow transition and runout distances of flowing avalanches. *Annals of Glaciology*, 18(1):221–226.

Savage, S. B. (1979). Gravity flow of cohesionless granular materials in chutes and channels. *Journal of Fluid Mechanics*, 92 part 1:53–96.

Savage, S. B. and Hutter, K. (1989). The motion of a finite mass of granular material down a rough incline. *Journal of Fluid Mechanics*, 199:177–215.

Schaerer, P. A. and Salway, A. A. (1980). Seismic and impact-pressure monitoring of flowing avalanches. *Journal of Glaciology*, 26:179–187.

Tai, Y.-C., Noelle, S., Gray, J. M. N. T., and Hutter, K. (2001). An accurate shock-capturing finite-difference method to solve the Savage-Hutter equations in avalanche dynamics. *Annals of Glaciology*, 32:263–267.

Whitham, G. B. (1999). *Linear and Nonlinear Waves*. John Wiley & Sons, Inc.